ELECTRONIC, MAGNETIC AND OPTICAL PROPERTIES OF GRAPHENE NANORIBBONS

A Thesis Submitted to
the Graduate School of Engineering and Sciences of
İzmir Institute of Technology
in Partial Fulfillment of the Requirements for the Degree of

MASTER OF SCIENCE

in Physics

by
Hakan Ulaş ÖZDEMİR

June 2016
İZMİR

We approve the thesis of **Hakan Ulaş ÖZDEMİR**

Examining Committee Members:

Assoc. Prof. Dr. Alev Devrim GÜÇLÜ
Department of Physics, İzmir Institute of Technology

Assoc. Prof. Dr. Özgür ÇAKIR
Department of Physics, İzmir Institute of Technology

Assoc. Prof. Dr. Cem SEVİK
Department of Mechanical Engineering, Anadolu University

27 June 2016

Assoc. Prof. Dr. Alev Devrim GÜÇLÜ
Supervisor, Department of Physics,
İzmir Institute of Technology

Prof. Dr. Ramazan Tuğrul SENGER
Head of the Department of
Physics

Prof. Dr. Bilge KARAÇALI
Dean of the Graduate School of
Engineering and Sciences

ACKNOWLEDGMENTS

I would like to thank my supervisor Assoc. Prof. Dr. Alev Devrim GÜÇLÜ for his endless and patience support. Even when I could not write a simple code, he was encouraging without making me feel inadequate. He is no less than a brother for me.

I have also much to thank to members of my defence committee, Assoc. Prof. Dr. Özgür ÇAKIR, Assoc. Prof. Dr. Cem SEVİK, Assoc. Prof. Dr. Haldun SEVİNÇLİ, Assoc. Prof. Dr. Ceyhun BULUTAY for helpful comments and suggestions.

In last two years, I was fortunate enough to meet and collaborate with great people. Working with Abdülmenaf ALTINTAŞ, Korhan Ertan ÇAKMAK was always a pleasure for me. Also I would like to send my warm regards to my roommates and my tea-crew: Kemal GÜLTEKİN, Halis GÜZELAYDIN and Özer ÖZDAL.

Finally, my parents Günel and Gürdal ÖZDEMİR were my endless source of love and motivation. They made this thesis possible.

ABSTRACT

ELECTRONIC, MAGNETIC AND OPTICAL PROPERTIES OF GRAPHENE NANORIBBONS

In this thesis, electronic, magnetic and optical properties of graphene nanoribbons are investigated within mean-field Hubbard model with two different disorder type; long and short range in finite and cyclic topology. First we investigated combined effect of electron-electron interaction effects and long range potential fluctuations. In both of the geometries, electron-electron interaction effects make edge states robust against disorders. Furthermore, surprisingly, strong enough disorder causes system to experience a phase transition from antiferromagnetically coupled edge states to ferromagnetic coupling in agreement with recent theoretical and experimental studies. Then, the stability of optical conductance under impurity effects, correlation between optical characteristic and magnetic phase of ZGNR is investigated, respectively. Similar to edge state density profile recovery, electronic interaction effects reduce the impurity induced peak around Fermi level. More importantly, we found distinct optical transitions due to edge-bulk mixed states around Fermi level that can be used to detect whether ZGNR is in antiferromagnetic or ferromagnetic phase. Finally, we investigated the disorder induced metal-insulator transition. Since, long range impurities protect the sublattice symmetry and leads to phenomena known as "absence of backscattering", there exist minimum conductivity for graphene. On the other hand, in order to model hydrogenation effects, we used short range impurity potential which breaks the sublattice symmetry. Using a time dependent tight binding model, we observed Anderson localization induced metal to insulator transition with a nanometer scale localization length for 2% hydrogen coverage. We found that, Anderson localization is stronger at high energy valence states since those states are more vulnerable to hydrogenation.

ÖZET

GRAFEN NANOŞERİTLERİN ELEKTRONİK, MANYETİK VE OPTİK ÖZELLİKLERİ

Bu tezde, ortalama-alan Hubbard modeli kullanarak zigzag kenarlı grafen nanoşeritlerin (ZGNŞ) elektronik, manyetik ve optik özelliklerini iki farklı geometride inceledik: sonlu ve çembersel. İlk olarak elektron-elektron etkileşiminin ve uzun mesafeli potansiyel düzensizliklerinin etkisi üzerine çalıştık. İki geometride de elektron-elektron etkileşiminin kenar durumlarını düzensizliklere karşı güçlü kıldığını ve şasırtıcı şekilde düzensizlik yeterince güçlü olduğunda antiferromanyetik durumdan ferromanyetik duruma faz geçişini tetiklediğini gördük. Bu sonuçlar, güncel kuramsal ve deneysel çalısmalarla örtüşmektedir. Daha sonra ZGNŞ'te düzensizliğin optik iletkenliğe etkisini inceledik. Önceki sonuçlarda olduğu gibi elektron-elektron etkileşiminin düzensizlik etkisini azalttığını gördük ve daha da önemlisi, Fermi seviyesine yakın bölgede bulunan kenar-yığın karışımı durumlar arası optik geçişten kaynaklanan soğurma karakteristiğinin sistemin manyetik fazını belirlemede kullanılabileceğini gösterdik. Son olarak, düzensizliklerin metal-yalıktan geçişine olan etkisini inceledik. Fakat, uzun mesafeli potansiyel dalgalanmaları alt-ağ simetrisini koruduğu ve geri saçılmadan yoksunlaştırdığı için, grafende minimum iletkenliğe sebep olurlar. Bu durumdan kurtulmak ve hidrojenlenme etkisini modelleyebilmek için, kısa mesafeli düzensizlikler kullandık ve alt-ağ simetrisini kırmayı başardık. Zamana bağlı sıkı bağlanma modeli kullanarak Anderson lokalizasyonunundan kaynaklı metal-yalıtkan geçişini nanometre düzeylerinde lokalizasyon uzunluğu olduğunu $\%2$ hidrojen kapsaması kullanarak gözlemledik. Anderson lokalizasyonun etkisinin yüksek enerjili valans bandlarında, düzensizlik durumlarinin bu bölgeye toplanmasından dolayı, diğer band bölgelerine göre daha fazla olduğunu gözlemledik.

TABLE OF CONTENTS

LIST OF FIGURES

Figure **Page**

CHAPTER 1

INTRODUCTION

Back in 1930s Landau and Peierls questioned the existence of 2D materials by showing that at any finite temperature oscillations due to thermal excitations exceed the interatomic distances. Therefore 2D systems should be thermodynamically unstable except at 0 K[1, 2]. Later experimental studies verified this result and 2D materials are only found as an integral part of 3D materials. Without such substrate, 2D crystals were literally thought to be nonexistence[4]. Contrary to these results, in 2004 graphene, first real 2D material was synthesized for the first time[5]. Following experimental studies showed that graphene is not perfectly flat, but it is crumpled in 3D. These height differences, so called ”corrugations” create strain and stabilize the lattice structure[7] in agreement with viewpoint of Landau and Peierls. From then on, interest on graphene is skyrocketed day by day. Figure 1.1 shows the number of scholar work those contain ”graphene” keyword per year between 2000 and 2015.

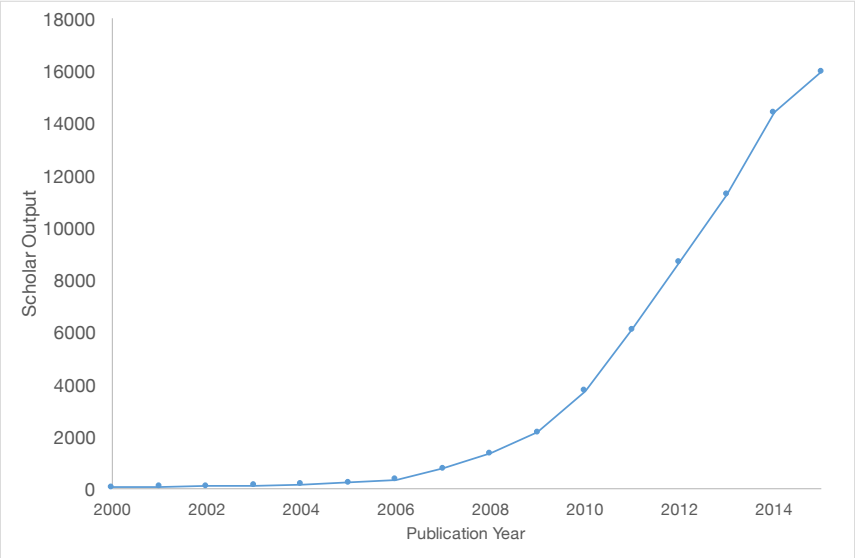

Figure 1.1. Scholar works contain ”graphene” in their title, abstract or keyword between the years 2000 and 2015. (Data obtained from SCOPUS)

Long before its discovery, graphene investigated by P. R. Wallace in 1947. There he showed, using a tight binding approach (TB), interesting properties such as linear dispersion relation around K and K' point and semimetallic behaviour[6]. Although there were other studies as well in last 50 years, graphene was not synthesized decade after its carbon allotropes successfully fabricated. These structures are shown in Figure 1.2.

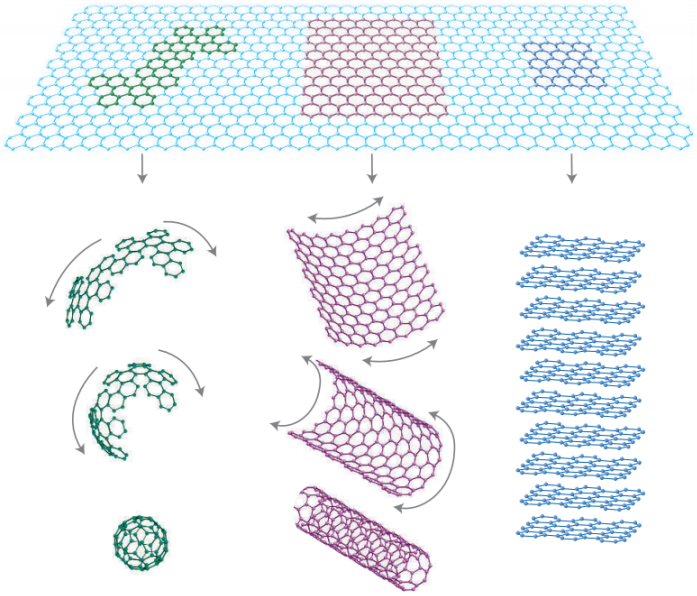

Figure 1.2. Nanostructures obtained from graphene. From left to right fullerene, carbon nanotube, graphite. Obtained from Reference [10]

One of the most extraordinary features of graphene is due to linear relation between momentum and energy. To explain the motion of electrons through a graphene sample Dirac equation may be solved, rather than Schrödinger equation [8–10] where both of the approaches give the same result around K and K' points. Having charge carriers similar to Dirac fermions provide unconventional properties to graphene. First one of these is the half integer quantum hall effect. 2D electron gas on perpendicular magnetic field is quantized with equally separated levels called "Landau levels"[11]. Although, quantum hall effect is observed in graphene at room temperature, quantized levels do not appear with equal spacing. Rather these states are spaced with half integer multiples of $\pm 2e^2/h$[12]. Another interesting property due to Dirac fermions is the Klein effect[13], where tunneling probability of an electron increases with potential height. This effect is also observed right after the discovery of graphene[14].

Although, it has numerous extraordinary properties, its gapless electronic struc-

ture prevent graphene to be used as a transistor. Therefore logic applications of it is highly limited. However, forbidden region in band structure can be introduced by constraining graphene along a direction [15–17]. Opening of the band gap is both theoretically and experimentally explained by relation between electronic interaction effects, edge termination and width of the nanoribbon [18–20]. Although both armchair and zigzag edge terminated graphene nanoribbons shows a band gap, it has been theoretically proposed many times[21–24], within Hubbard model zigzag graphene nanoribbons is expected to have spin polarized edges which should give rise to magnetism in agreement with Lieb's theorem [25]. In his work, Lieb showed, in a bipartite lattice, half of the difference between number of each sublattice corresponds to ground state magnetic moment. Thus ground state of the perfect zigzag graphene nanoribbons should have antiferromagnetically coupled edges where $S_z = 0$. This property makes zigzag graphene nanoribbons a powerful candidate for future spintronic applications. In 2006 Son *et al.* showed that it is possible to filter out one spin orientation by applying electric field along finite direction which enlarges band gap for one spin orientation and reduces gap for the oppsite one. Therefore system is insulator for a spin orientation, but conductor for other electrons with opposite one. This phenomena named as half-metallicity. Later, it was shown that spin injection is possible by introducing single edge disorders those halt the diffusion of one of the spin states[26]. However, experimentally induced edge magnetization still could not be observed, probably due to limited control over edge geometry. In March 2016, a group managed to synthesize narrow, long and disorder free ZGNRs by using polymerization and cyclohydrogenation [28]. In addition to that, an indirect observation of magnetic phase transition is observed by analyzing the relation between energy gap and width of the ribbon [20]. These recent developments raised hope for potential graphene based spintronic devices.

Magnetism is mostly believed to be originated from d and f orbitals. However, earlier studies showed that disorders in graphene may lead to room-temperature magnetism even though carbon itself is not magnetic. Source of this magnetism is not directly related to d and f orbitals. Rather these can be explained by vacancy induced small zigzag edge domains [29, 32]. These studies created a new research branch in physics: carbon based magnetism that is superior to metallic magnetism due to long spin relaxation lengths [30, 31].

The observation of a magnetic phase transition in graphene nanoribbons along zigzag edges is a surprising result due to the experimental difficulties for fabricating clean nanostructures with properly passivated and well defined edges[33–37], and free from im-

perfections in the lattice or in the substrate. A possible source of irregularity in a graphene structure is the formation of the so-called electron-hole puddles [38–41]. Those highly inhomogeneous charge distributions were observed by Martin *et al*[42]. by mapping the charge neutrality point. Later, Crommie *et al.* [43] reported that impurities between the substrate and the graphene sheet induce a distorted electron liquid, which is in agreement with earlier theoretical works as well[39, 45]. A different study stated that corrugations are the mechanism behind the formation of charge inhomogeneities [44].

Another fascinating feature is the strong optical absorption of single layer graphene, even visible under optical microscope. In 2008, it was concluded that fine structure constant $e^2/\hbar c$ [46] directly corresponds to absorption of graphene and independent of any other property[47]. Fine structure constant is one the most fundamental constants of quantum mechanics and probing of it is possible only by using highly specific equipment. However, optical absorption of graphene enables scientists to measure this quantity by only using an optical microscope[48].

This thesis is organized as follow. In the next chapter graphene fundamentals are introduced. First part of this chapter is devoted to fabrication methods of graphene, starting from the first and the most basic technique known as exfoliations, chemical vapor deposition (CVD) and thermal decomposition of SiC are introduced. After that, theoretical tools we have used for this study are introduced and explained in deep starting from tight binding foundations of graphene, then more realistic spin dependent mean-field Hubbard Hamiltonian is derived. Since it is impossible to fabricate a perfect graphene, by its very nature disorders exist in graphene. In the next section sources of these disorders are introduced. First, effect of edge geometry then charged impurities are discussed. In this section, details about modeling of the two different impurity sources, long range smooth potentials and hydrogenation of $2p_z$ orbitals are explained in deep. Next section is devoted to one of the most intriguing properties of graphene which is minimum optical conductivity. For both of the finite and cyclic structures the exact same antiferromagnetic to ferromagnetic phase transition is observed under impurity effects. Finally, phenomena known as metal-insulator transition due to impurity effects, known as Anderson localization is theoretically explained, then calculation details are given. Due to geometrical constraints, Anderson localization and optical conductivity invesitgation are only performed for finite system. Final section contains a brief summary of this work.

CHAPTER 2

GRAPHENE

In this chapter, fabrication techniques, theoretical models used in this work, sources of disorders, metal insulator transition due to Anderson localization and optical conductivity on graphene is presented.

2.1. Fabrication Techniques

In section below, several ways to obtain graphene and graphene nanoribbon samples to use in devices are described. A few large scale production methods are also presented and a recent ZGNR fabrication method is explained briefly.

Mechanical Exfoliation This is the first and the simplest way of obtaining graphene, as known as "Scotch Tape Method", used by Geim and his group in 2004. In this method, a few layers of graphene can be extracted by sticking adhesive tape on to graphite crystal. Sticky force of adhesive tape overwhelms the weak van der Waals forces those bound graphene layers together. Having peel the tape off, leaves a few layers of graphene. Sticking the tape on to itself couple of times make layers thinner gradually. After that, the tape should be pressed on a substrate, typically SiO_2, then peeled off. There is a possibility to have single layer graphene islands on substrate which can be distinguished by lighter and darker regions visible under optical microscope. Although scotch tape method allows scientist to create samples with high crystal quality, most of the time products get as big as $\mu\mathrm{m}$ scale which is very small in size for applications except laboratory usage. Control over the sample size also very limited. Figure 2.1 shows graphene samples under optical microscope fabricated with this method.

Liquid-phase Exfoliation To exploit graphene in daily life applications large amount of material should be obtained. One way to achieve this is to use organic solvents like N-methyl-pyrrolidone whose surface energy matches with exfoliation energy of graphite. Next, high voltage or high frequency ultrasound is applied to solution. Then, in order to get rid of thick layers, solution has to centrifuged. Similar to mechanical exfoliation,

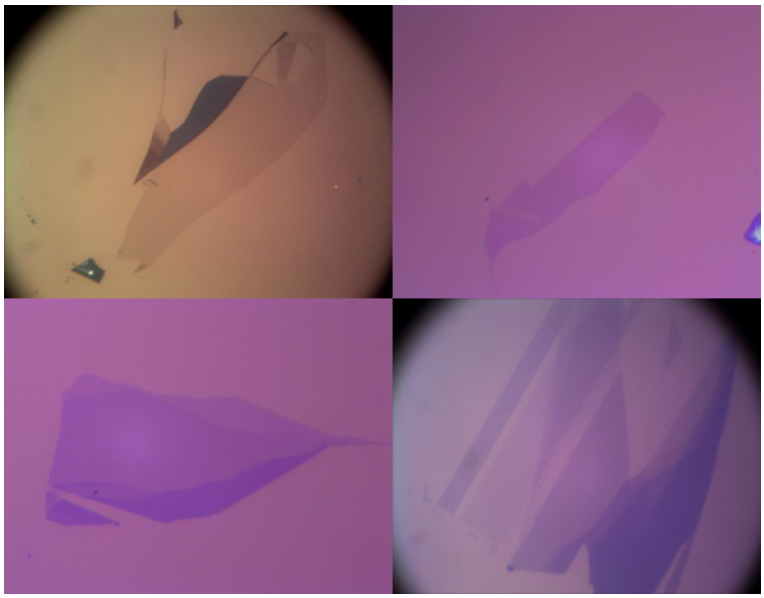

Figure 2.1. Graphene samples under optical microscope. Lighter and darker regions shows single and a few layers of graphene sheets respectively.(Obtained from *http://www.graphene.ac.rs/exfoliation.html*)

although product contains almost no defects or impurities, size is still small for possible applications. In Figure 2.2 production steps are shown. Similar to preceding ones, controlled production is not possible with this method.

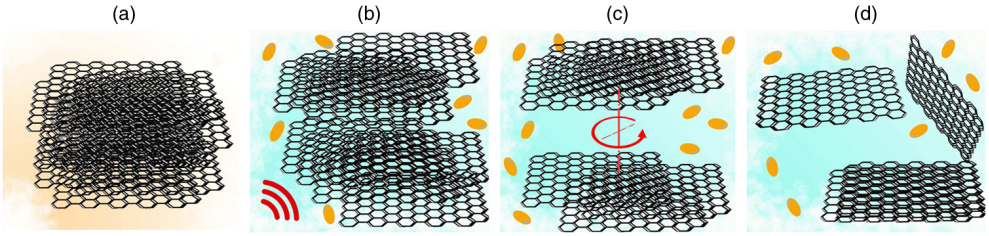

Figure 2.2. Fabrication steps of liquid-phase exfoliation of graphite.Obtained from [49]

Graphite Oxide Exfoliation Graphite oxide can be solved in liquids due to its several functional groups. As a result, graphene layers becomes negatively charged and repels each other. Then similar to liquid-phase exfoliation, by centrifuging the sample one can obtain graphene oxide. To extract clean graphene, several chemical and thermal processes should be applied. However, quality of crystal is low because of the oxygen remnants.

Compared to preceding methods, extracting graphene from graphite oxide exfoliation is complicated because of the several production steps. But if the desired product is graphene oxide, this method might be the most efficient one.

Chemical Vapor Decomposition (CVD) Other well known method is based on catalytic metals such as nickel and iron. When methane is exposed to these metal films under high temperature, hydrogen evaporates and leaves only carbon atoms. Remnant carbons diffuses into catalytic metal and upon cooling down in Ar rich atmosphere, graphene layer grows on metallic surface. Number of layers achieved with this method strictly depends on thickness of the catalytic metal film that can be controllable. One of the main advantages is, shape of the resultant graphene is the same with metallic film layer. Thus one can control shape of the product by modifying the catalytic metal. Then, metallic film can be etched and bare graphene sheet can be transferred to substrate. It is also known that using different metal layers (Cu instead of Ni), changes the efficiency of the production.

Thermal decomposition of SiC Single or a few layers of graphene can be obtained by heating SiC wafers. Si releases from the surface when the sample is heated up and left over carbon atoms form graphene which first showed by Berger and co-workers[50]. In addition to synthesizing a few layers of graphene, they showed Dirac like behavior of charge carriers with mobility exceeding $25000\ cm^2\ V^{-1}\ s^{-1}$. Then, Ohta[51] and coworkers revealed linear dispersion relation around K point using angle-resolved photoemission spectroscopy (ARPES). Up to this point, production was taking place in ultra high vacuum that leads to low crystal quality and inhomogeneous graphene distribution. In 2008, homogeneous graphene is obtained by adding argon to reaction environment which alters the growth kinetics, reduces the decomposition hence leads to high quality graphene[52]. Upside of using this technique is to ability to tailor structures like nanoribbons and dots with widespread lithographic methods.

Surface Assisted Polymerization Although top-down approaches to produce disorder free, long ZGNRs failed until today[15, 17, 20, 53, 54], recently a group managed to fabricate it by using bottom-up synthesis[28]. This method is based on Au(111) surface assisted polymerization and cyclohydrogenation of U shaped base monomer that is produced by organic synthesis. As expected, in this work edge states are successfully observed by using scanning tunneling spectroscopy. Fig 2.3(a) shows a long, disorder free ZGNR produced by this method. On the other hand (b) and (c) compares the observed and theoretical DFT based edge states.

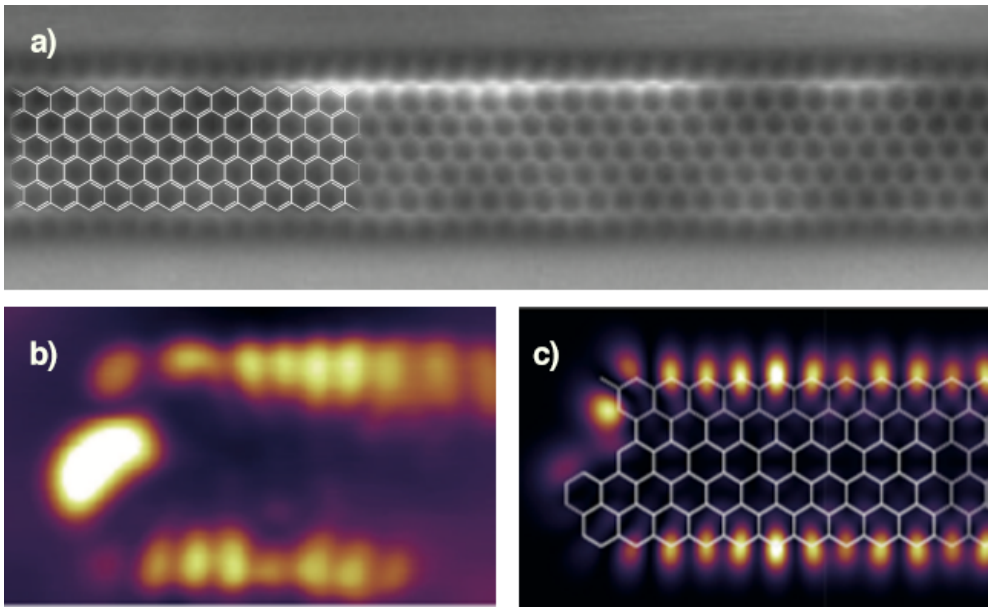

Figure 2.3. (a) Fabricated long, disorder-free ZGNR. (b) Edge states observed by scanning tunneling spectroscopy. (c) DFT based edge states. Obtained from [28]

2.2. Theoretical Foundations

Graphene has been investigated by using several theoretical models such as, tight binding, Hubbard, mean-field theories density functional theory (DFT) and molecular dynamics (MD) approaches[34, 40, 45, 55]. In this study we are going to exploit tight binding and mean-field Hubbard models due to two main reasons. First,although graphene has four valence electrons, three of which are used to make bonds with neighbor carbon atoms. Thus, single p_z orbital approach is proved to be highly accurate for determining the electronic properties of graphene. Second, these two model gives us the possibility to create a very large system with up to ten thousand atoms. While, other methods are limited about hundred atoms.

2.2.1. Tight-Binding Model

One of the most fundamental yet accurate way of understanding the electronic structure of materials is called tight binding model where it is assumed there exist localized orbitals at each atomic sites. Thus total electronic wavefunction can be written as

superposition of these localized orbitals

$$\psi(\vec{r}) = \sum_i C_i \phi_i(\vec{r} - \vec{r}_i) \tag{2.1}$$

Then, problem reduces to finding $C_i's$. In order to find them, one has to solve time-independent Schrödinger equation as follows,

$$\hat{H}\psi(\vec{r}) = E\psi(\vec{r}) \tag{2.2}$$

Multiplying from left by $\langle\phi_i|$ and extending in terms of localized orbitals.

$$\langle\phi_i| \hat{H} |\psi\rangle - E \langle\phi_i|\psi\rangle = 0 \tag{2.3}$$

$$\sum_n C_n(\langle\phi_i| \hat{H} |\phi_n\rangle - E \langle\phi_i|\phi_n\rangle) = 0 \tag{2.4}$$

To simplify the problem, one can limit the interacting by only considering nearest neighbor atoms. Now summation is limited with only neighbor atoms.

$$\sum_{<n,i>} C_n(\langle\phi_i| \hat{H} |\phi_n\rangle - E \langle\phi_i|\phi_n\rangle) = 0 \tag{2.5}$$

where $< n, i >$ indicates summation is over nearest neighbor atoms where integrals $\langle\phi_i| \hat{H} |\phi_n\rangle = t$, $\langle\phi_i|\phi_n\rangle = 0$, $\langle\phi_n|\phi_n\rangle = 1$ when $i \neq n$.

If there is translational symmetry one can exploit Bloch theorem to write wave-function as,

$$\psi_k(\vec{r}) = \frac{1}{\sqrt{N}} \sum_i e^{i\vec{k}\cdot\vec{r}_i} \phi(\vec{r} - \vec{r}_i) \tag{2.6}$$

The electronic structure of graphene investigated by P.R Wallace in 1946[6]. In his paper, titled "The Band Theory of Graphite" Wallace made two major assumptions. First, the large spacing between graphene layers compared to inter-carbon distance on plane, confines electron to move only in the plane.

Carbon atom has 4 valence electrons, where three of these occupy $2s$, $2p_x$, $2p_y$ orbitals which forms sp^2 bonds with surrounding carbon atoms on plane and responsible with mechanical properties of graphene sheet. The last electron fills the p_z orbital. This orbital resides perpendicular to surface and forms π bonds. The second assumption is that,

electronic properties of graphene can be described by only using p_z orbital within tight-binding approximation. Although tight binding model does not take electron-electron interaction into account, it gives highly accurate results for graphene.

Lattice structure of graphene can be defined by using two sublattices with spacing between them $b = 1.42\mathring{A}$ and lattice vectors can be defined as $a_{1,2} = \pm\frac{a\sqrt{3}}{2}\hat{\imath}, \frac{3a}{2}\hat{\jmath}$

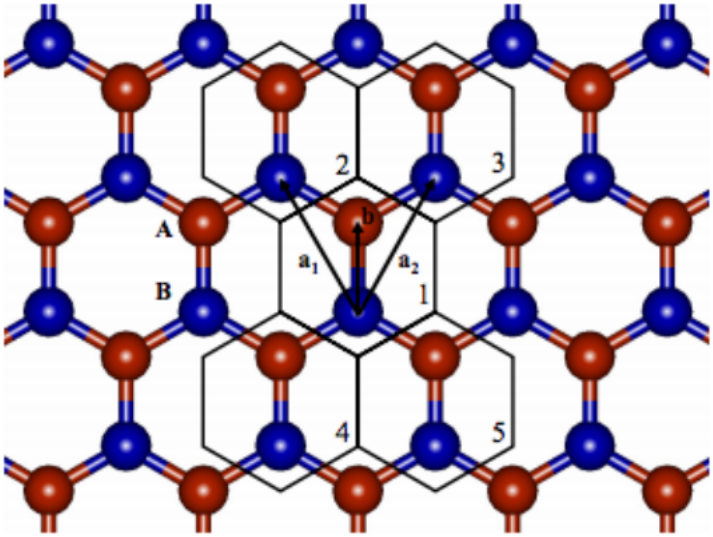

Figure 2.4. Lattice structure of graphene contains two atom labeled with A and B in its unit cell. Obtained from [87]

One can define total electron wavefunction by superposition of bipartite lattice wavefunctions.

$$\Psi_i(r) = A_i\psi_i^A(r) + B_i\psi_i^B(r) \tag{2.7}$$

The wavefunction of an electron on A sublattice can be discretized in terms of p_z orbitals.

$$\psi_i^A(r) = \frac{1}{\sqrt{N_A}}\sum_{r_a} e^{ikr_a}\phi_{2p_z}(r - r_a) \tag{2.8}$$

Similarly,

$$\psi_i^B(r) = \frac{1}{\sqrt{N_B}}\sum_{r_b} e^{ikr_b}\phi_{2p_z}(r - r_b) \tag{2.9}$$

where N is the number of A and B sublattice sites.

To solve the system, one need to plug Eqn. (2.7) into time independent Schrödinger equation and multiply from the left side both of the p_z orbitals.

$$\left\langle \psi_i^A \right| \hat{H} \left| \Psi_i \right\rangle = \left\langle \psi_i^A \middle| \Psi_i \right\rangle \tag{2.10}$$

$$\left\langle \psi_i^B \right| \hat{H} \left| \Psi_i \right\rangle = \left\langle \psi_i^B \middle| \Psi_i \right\rangle \tag{2.11}$$

Since interaction between atoms limited with nearest neighbor sites and on site energies are neglected, one can have,

$$\begin{aligned} \left\langle \psi_i^A \right| \hat{H} \left| \psi_i^A \right\rangle &= 0 \\ \left\langle \psi_i^B \right| \hat{H} \left| \psi_i^B \right\rangle &= 0 \end{aligned} \tag{2.12}$$

However, hopping integral between nearest neighbor terms $\left\langle \psi_i^A \right| \hat{H} \left| \psi_i^B \right\rangle$ and $\left\langle \psi_i^B \right| \hat{H} \left| \psi_i^A \right\rangle$ has the following form,

$$\left\langle \psi_i^A \right| \hat{H} \left| \psi_i^B \right\rangle = \frac{1}{N} \sum_{<r_A, r_B>} e^{i\vec{k}\cdot(\vec{r}_A - \vec{r}_B)} \int d\vec{r} \phi^*_{2p_z}(\vec{r} - \vec{r}_B) H(\vec{r} - \vec{r}_B) \phi_{2p_z}(\vec{r} - \vec{r}_A). \tag{2.13}$$

By approximating hopping integrals from A to B and B to A are the same and value is constant t.

$$t = \int d\vec{r} \phi^*_{2p_z}(\vec{r} - \vec{r}_B) H(\vec{r} - \vec{r}_B) \phi_{2p_z}(\vec{r} - \vec{r}_A), \quad t_{nn} \approx -2.8 \quad \text{and} \quad t_{nnn} = -0.1eV \tag{2.14}$$

where t_{nn} and t_{nnn} denotes the first and second nearest neighbor hopping parameters respectively. Knowing that, three nearest neighbor vectors are $\vec{a}_1 = \frac{a}{\sqrt{3}}\hat{\imath}$,$\vec{a}_2 = \frac{a}{\sqrt{3}}(\frac{-1}{2}\hat{\imath} + \frac{3}{2}\hat{\jmath})$, $\vec{a}_3 = \frac{a}{\sqrt{3}}(\frac{-1}{2}\hat{\imath} - \frac{3}{2}\hat{\jmath})$.

$$\begin{aligned} \left\langle \psi_i^A \right| \hat{H} \left| \psi_i^B \right\rangle &= t(e^{-i\vec{k}\cdot\frac{a}{\sqrt{3}}\hat{\imath}} + e^{-i\vec{k}\cdot\frac{a}{\sqrt{3}}(\frac{-1}{2}\hat{\imath}+\frac{3}{2}\hat{\jmath})} + e^{-i\vec{k}\cdot\frac{a}{\sqrt{3}}(\frac{-1}{2}\hat{\imath}-\frac{3}{2}\hat{\jmath})}) \\ \left\langle \psi_i^B \right| \hat{H} \left| \psi_i^A \right\rangle &= t(e^{i\vec{k}\cdot\frac{a}{\sqrt{3}}\hat{\imath}} + e^{i\vec{k}\cdot\frac{a}{\sqrt{3}}(\frac{-1}{2}\hat{\imath}+\frac{3}{2}\hat{\jmath})} + e^{i\vec{k}\cdot\frac{a}{\sqrt{3}}(\frac{-1}{2}\hat{\imath}-\frac{3}{2}\hat{\jmath})}) \end{aligned} \tag{2.15}$$

It is easy to see that,

$$\left\langle \psi_i^A \right| \hat{H} \left| \psi_i^B \right\rangle = \left\langle \psi_i^B \right| \hat{H} \left| \psi_i^A \right\rangle^* \tag{2.16}$$

Now problem is reduced to an eigenvalue, eigenvector problem. Write two equations in matrix form,

$$E \begin{bmatrix} A_k \\ B_k \end{bmatrix} = \begin{bmatrix} 0 & tf_k \\ tf_k^* & 0 \end{bmatrix} \begin{bmatrix} A_k \\ B_k \end{bmatrix} \tag{2.17}$$

Solution of this system is,

$$E = \pm|t\vec{f}_k| \quad \text{where} \quad \vec{f}_k = (e^{-i\vec{k}\cdot\frac{a}{\sqrt{3}}\hat{\imath}} + e^{-i\vec{k}\cdot\frac{a}{\sqrt{3}}(\frac{-1}{2}\hat{\imath}+\frac{3}{2}\hat{\jmath})} + e^{-i\vec{k}\cdot\frac{a}{\sqrt{3}}(\frac{-1}{2}\hat{\imath}-\frac{3}{2}\hat{\jmath})}) \tag{2.18}$$

Equation 2.18 shows that energy is linearly related to momentum which is a property of massless Dirac fermions. Fig. 2.5 shows the band structure obtained from dispersion relation above. Moreover pseudospins can be written as,

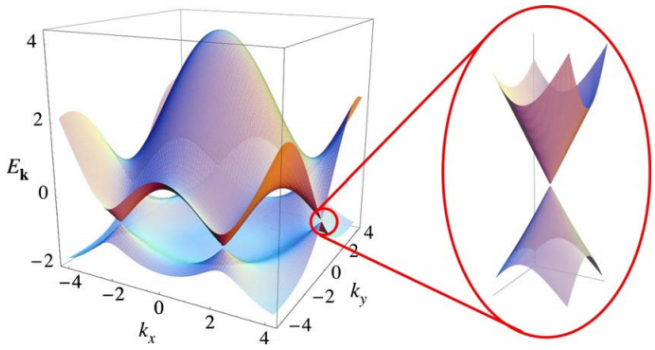

Figure 2.5. Band structure of graphene. Obtained from [9]

$$\begin{bmatrix} A_k \\ B_k \end{bmatrix} = \frac{1}{\sqrt{2}} \begin{bmatrix} 1 \\ \frac{-f^*(\vec{(k)})}{f(\vec{k})} \end{bmatrix} \quad \text{and} \quad \begin{bmatrix} A_k \\ B_k \end{bmatrix} = \frac{1}{\sqrt{2}} \begin{bmatrix} 1 \\ \frac{+f^*(\vec{(k)})}{f(\vec{k})} \end{bmatrix} \tag{2.19}$$

Above solution is valid for bulk graphene. However, for finite system one has to employ a different method to get the electronic structure. First, Hamiltonian matrix whose size is NxN should be declared where N is the number of atoms. Then, this matrix is filled with respect to neigboring atoms, whether these atoms are first (t_{nn}), second(t_{nnn}) or distant neighbors.

2.2.2. Mean-Field Hubbard Model

Although TB model gives pretty accurate results, it has no spin dependence and electronic correlation effects. Hence gives no information about true filling of the states

and magnetic properties. One can overcome this by solving many-body problem. However, without any good approximation, only very basic systems are exactly solvable (1D Ising model etc.). Therefore many-body problem can be reduced to one body problem by introducing a "molecular background field" that is the mean-field created by all particles. This system only solvable self-consistently.

Now starting from exact many-bond Hamiltonian we are going to derive mean-field Hubbard Hamiltonian.

$$H = \sum_{pq} t_{pq} c_p^\dagger c_q + \frac{1}{2} \sum_{pqrs} (pq|V|rs) c_p^\dagger c_q^\dagger c_r c_s \tag{2.20}$$

For the first term, where $p = i\sigma$, $q = j\sigma'$ and σ indicates spin dependence.

$$t_{pq} = \langle p| \, t \, |q\rangle = \langle i\sigma| \, t \, |\sigma' j\rangle = \langle i| \, t \, |j\rangle \underbrace{\langle \sigma|\sigma'\rangle}_{\delta_{\sigma\sigma'}} \tag{2.21}$$

Similarly for interaction term, $p = i\sigma$, $q = j\sigma'$, $r = k\sigma''$, $s = l\sigma'''$

$$V_{i,j} = \frac{1}{2} \sum_{pqrs} (pq|V|rs) c_p^\dagger c_q^\dagger c_r c_s = \frac{1}{2} \sum_{ijkl} \langle ij| \, V \, |kl\rangle \, c_i^\dagger c_j^\dagger c_k c_l \underbrace{\langle \sigma|\sigma'''\rangle}_{\delta_{\sigma\sigma'''}} \underbrace{\langle \sigma'|\sigma''\rangle}_{\delta_{\sigma'\sigma''}} \tag{2.22}$$

Finally, Eqn. 2.20 can be written as,

$$H = \sum_{ij} t_{ij} c_{i\sigma}^\dagger c_{j\sigma} + \frac{1}{2} \sum_{ijkl} \langle ij| \, V \, |kl\rangle \, c_{i\sigma}^\dagger c_{j\sigma'}^\dagger c_{k\sigma'} c_{l\sigma} \tag{2.23}$$

Next, to calculate on-site repulsion term say that

$$\langle ii| \, V \, |ii\rangle = U \quad \text{and} \quad \frac{1}{2} \sum_{ijkl} \langle ij| \, V \, |kl\rangle \, c_{i\sigma}^\dagger c_{j\sigma'}^\dagger c_{k\sigma'} c_{l\sigma} = \frac{1}{2} \sum_{i\sigma\sigma'} U c_{i\sigma}^\dagger c_{i\sigma'}^\dagger c_{i\sigma'} c_{i\sigma} \tag{2.24}$$

After expanding the spin terms and exploiting the second quantization algebra, final on

site expression becomes,

$$\frac{U}{2}\sum_{i}\underbrace{c_{i\uparrow}^{\dagger}c_{i\uparrow}}_{n_{i\uparrow}}\underbrace{c_{i\downarrow}^{\dagger}c_{i\downarrow}}_{n_{i\downarrow}}+c_{i\downarrow}^{\dagger}c_{i\downarrow}c_{i\uparrow}^{\dagger}c_{i\uparrow}=U\sum_{i}n_{i\uparrow}n_{i\downarrow} \tag{2.25}$$

Likewise for off-site repulsion term,

$$\langle ji|\,V\,|ij\rangle = V_{ij} \quad and \quad \frac{1}{2}\sum_{\substack{i\neq j\\ \sigma\sigma'}}\langle ji|\,V\,|ij\rangle\, c_{i\sigma}^{\dagger}c_{j\sigma'}^{\dagger}c_{j\sigma}c_{i\sigma'} \tag{2.26}$$

Again using the properties $\{c_{i\sigma}, c_{j\sigma'}\} = 0$ and $\{c_{j\sigma'}^{\dagger}, c_{i\sigma}\} = \delta_{i,j}\delta_{\sigma\sigma'}$

$$\begin{aligned}
\frac{1}{2}\sum_{\substack{i\neq j\\ \sigma\sigma'}}V_{ij}c_{i\sigma}^{\dagger}c_{\jmath\sigma'}^{\dagger}(-c_{i\sigma}c_{\jmath\sigma'}) &= \frac{1}{2}\sum_{\substack{i\neq j\\ \sigma\sigma'}}V_{ij}c_{i\sigma}^{\dagger}(-\delta_{\sigma\sigma'}\underbrace{\delta_{ij}}_{\substack{=0\\ i\neq j}}+c_{i\sigma}c_{j\sigma'}^{\dagger})c_{j\sigma'}\\
&= \frac{1}{2}\sum_{\substack{i\neq j\\ \sigma\sigma'}}V_{ij}n_{i\sigma}n_{j\sigma'}\\
&= \frac{1}{2}\sum_{ij}V_{ij}(n_{i\uparrow}n_{j\uparrow}+n_{i\downarrow}n_{j\downarrow}+n_{i\uparrow}n_{j\downarrow}+n_{i\downarrow}n_{j\uparrow})\\
&= \frac{1}{2}\sum_{ij}V_{ij}\underbrace{(n_{i\uparrow}+n_{i\downarrow})}_{n_i}\underbrace{(n_{j\uparrow+n_{j\downarrow}})}_{n_j} = \frac{1}{2}\sum_{i\neq j}V_{ij}n_in_j
\end{aligned} \tag{2.27}$$

Finally Hubbard and extended Hubbard Hamiltonian can be written as summation of all terms.

$$H = \underbrace{\underbrace{\sum_{\substack{ij\\ \sigma}}t_{ij}c_{i\sigma}^{\dagger}c_{j\sigma}+U\sum_{i}n_{i\uparrow}n_{i\downarrow}}_{\text{Hubbard Model}}+\frac{1}{2}\sum_{i\neq j}V_{ij}n_in_j}_{\text{Extended Hubbard Model}} \tag{2.28}$$

Now exact Hamiltonian is derived, we can begin derivation of mean-field Hubbard Hamiltonian by defining,

$$n_{i\uparrow} = \langle n_{i\uparrow}\rangle + \underbrace{(n_{i\uparrow}-\langle n_{i\uparrow}\rangle)}_{\Delta n_{i\uparrow}} \quad \text{and} \quad n_{i\downarrow} = \langle n_{i\downarrow}\rangle + \underbrace{(n_{i\downarrow}-\langle n_{i\downarrow}\rangle)}_{\Delta n_{i\downarrow}} \tag{2.29}$$

$$n_{i\sigma} = \langle n_{i\sigma} \rangle + \underbrace{(n_{i\sigma} - \langle n_{i\sigma} \rangle)}_{\Delta n_{i\sigma}} \quad \text{and} \quad n_{j\sigma} = \langle n_{j\sigma} \rangle + \underbrace{(n_{j\sigma} - \langle n_{j\sigma} \rangle)}_{\Delta n_{j\sigma}} \tag{2.30}$$

For on-site term using Eq. 2.29.,

$$\begin{aligned} n_{i\uparrow} n_{i\downarrow} =& [\langle n_{i\uparrow} \rangle + \Delta n_{i\uparrow}][\langle n_{j\sigma} \rangle + \Delta n_{i\downarrow}] \\ & \langle n_{i\uparrow} \rangle \langle n_{i\downarrow} \rangle + \langle n_{i\uparrow} \rangle \Delta n_{i\downarrow} + \Delta n_{i\uparrow} \langle n_{i\downarrow} \rangle + \underbrace{\Delta n_{i\uparrow} \Delta n_{i\downarrow}}_{\approx 0} \\ & \approx \langle n_{i\uparrow} \rangle n_{i\downarrow} + \langle n_{i\downarrow} \rangle n_{i\uparrow} - \langle n_{i\uparrow} \rangle \langle n_{i\downarrow} \rangle \end{aligned} \tag{2.31}$$

By using Eq. 2.30. similar to preceding calculation off-site repulsion term becomes,

$$n_i n_j \approx \langle n_i \rangle n_j + \langle n_j \rangle n_i - \langle n_i \rangle \langle n_j \rangle \tag{2.32}$$

Finally Hamiltonian can be approximated by,

$$\begin{aligned} H \approx & \sum_{ij\sigma} t_{ij} c^{\dagger}_{i\sigma} c_{j\sigma} + U \sum_i \langle n_{i\uparrow} \rangle n_{i\downarrow} + \langle n_{i\downarrow} \rangle n_{i\uparrow} - \langle n_{i\uparrow} \rangle \langle n_{i\downarrow} \rangle \\ & + \frac{1}{2} \sum_{i \neq j} V_{ij} \langle n_i \rangle n_j + \langle n_j \rangle n_i - \langle n_i \rangle \langle n_j \rangle \end{aligned} \tag{2.33}$$

Our t_{ij} value is calculated within mean-field theory[9], however, t_{ij} in Eq. 2.32 is not related to this model. Thus we need to calculate mean field t_{ij} which we will call τ_{ij} Now we are going to assume that, system interacts with a constant background charge field and their values are,

$$\langle n_i \rangle = 1 \quad \text{and} \quad \langle n_{i\sigma} \rangle = \frac{1}{2} \tag{2.34}$$

which makes bulk mean field Hamiltonian,

$$H^{Bulk}_{MF} = \sum_{ij\sigma} t_{ij} c^{\dagger}_{i\sigma} c_{j\sigma} - \frac{U}{2} \sum_i (n_{i\uparrow} + n_{i\downarrow} - \frac{1}{2}) - \frac{1}{2} \sum_{ij} V_{ij} (n_i + n_j - 1) \tag{2.35}$$

To get the single body mean field Hubbard Hamiltonian, we are going to use

$$
\begin{aligned}
H_{MF} &= H_{MF} - H_{MF}^{Bulk} + H_{MF}^{Bulk} \\
&= \cancelto{0}{\sum_{ij\sigma} t_{ij} c_{i\sigma}^{\dagger} c_{j\sigma}} + U \sum_i \langle n_{i\uparrow} \rangle n_{i\downarrow} + \langle n_{i\downarrow} \rangle n_{i\uparrow} - \langle n_{i\uparrow} \rangle \langle n_{i\downarrow} \rangle \\
&+ \frac{1}{2} \sum_{i \neq j} V_{ij} \langle n_i \rangle n_j + \langle n_j \rangle n_i - \langle n_i \rangle \langle n_j \rangle \\
&- \cancelto{0}{\sum_{ij\sigma} t_{ij} c_{i\sigma}^{\dagger} c_{j\sigma}} - \frac{U}{2} \sum_i (n_{i\uparrow} + n_{i\downarrow} - \frac{1}{2}) - \frac{1}{2} \sum_{ij} V_{ij} (n_i + n_j - 1) \\
&+ \sum_{ij\sigma} t_{ij} c_{i\sigma}^{\dagger} c_{j\sigma} + \frac{U}{2} \sum_i (n_{i\uparrow} - n_{i\downarrow} - \frac{1}{2}) - \frac{1}{2} \sum_{ij} V_{ij} (n_i + n_j - 1) \\
&= \underbrace{\sum_{ij\sigma} t_{ij} c_{i\sigma}^{\dagger} c_{j\sigma} + \frac{U}{2} \sum_i (n_{i\uparrow} + n_{i\downarrow}) + \frac{1}{2} \sum_{ij} V_{ij} (n_i + n_j)}_{\sum_{\langle ij\sigma \rangle} \tau_{ij} (c_{i\sigma}^{\dagger} c_{j\sigma} + H.c)} \\
&+ U \sum_i [(\langle n_{i\uparrow} \rangle - \frac{1}{2}) n_{i\downarrow} + \langle n_{i\downarrow} \rangle - \frac{1}{2}) n_{i\uparrow}] \\
&+ \frac{1}{2} \sum_{ij} V_{ij} [\langle n_i \rangle - \frac{1}{2}) n_j + \langle n_j \rangle - \frac{1}{2}) n_i] + \cancelto{0}{Constants}
\end{aligned}
\tag{2.36}
$$

Finally knowing that $V_{ij} = V_{ji}$, mean field Hamiltonian becomes its last form as follow.

$$
\begin{aligned}
H_{MFH} = &\sum_{i,j,\sigma} \tau_{ij} (c_{i,\sigma}^{\dagger} c_{j,\sigma} + h.c) + U \sum_i (\langle n_{i,\uparrow} \rangle - \frac{1}{2}) n_{i\downarrow} + (\langle n_{i,\downarrow} \rangle - \frac{1}{2}) n_{i\uparrow} \\
&+ \sum_{i,j} V_{ij} [(\langle n_i \rangle - 1) n_j + (\langle n_j \rangle - 1) n_i]
\end{aligned}
\tag{2.37}
$$

2.3. Sources of Disorder in Graphene

2.3.1. Edge Effects

Creating a graphene nanostructure from a bulk sample generates different kind of boundaries depending on the cutting axis. There are two major edge patterns; zigzag and armchair edges. Electronic property of nanostructure highly depend on these edge terminations. Bulk graphene is a gapless semi-metal which makes it useless for micro-

electronic device applications. However it is possible to induce energy gap by introducing edge termination. Although, it is experimentally hard to create disorder free edges, latest studies showed that both narrow AGNR and ZGNR can be fabricated by polymerization and subsequent cyclodehydrogenation on Au(111) substrate[27, 28].

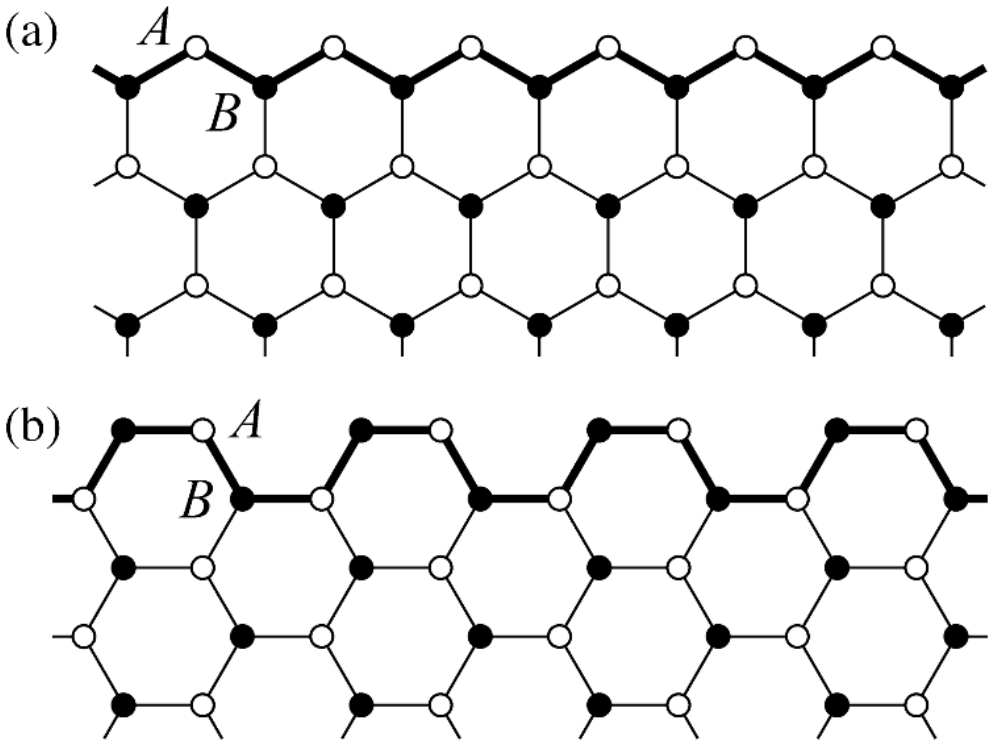

Figure 2.6. Two major edge geometry of graphene nanostructures. (Obtained from [69])

Zigzag edges naturally show broken sublattice symmetry. This feature gives zigzag edges a remarkable feature, lowest energetic conduction bands and highest energetic valence bands are degenerate within $k = [\pi, 2\pi/3]$ region. These states are called edge states(flat bands,zero energy states...) are localized strictly at the zigzag boundaries forms a sharp DOS peak around Fermi level. Localization can be found analytically by solving a TB system which is first solved by Nakada *et. al.*[19] By assigning atomic orbitals components of a Bloch wavefunction in the form $e^{ikn}, e^{ik(n-1)}$ where n stands for location of site on edge. In nearest neighbor hopping only TB calculation, every column or row of Hamiltonian should contain three nonzero elements. Thus if we are to solve

time-independent Schrödinger equation as follow.

$$\begin{bmatrix} \ddots & \dots & \dots & \dots & \dots & \dots \\ \vdots & t_{m-1,m} & 0 & t_{m+1,m} & t_{m+2,m} & \dots \\ \vdots & \vdots & \vdots & \ddots & \vdots & \dots \\ \dots & \dots & \dots & \dots & \dots & \dots \end{bmatrix} \begin{bmatrix} \vdots \\ a_{m-1} \\ a_m \\ a_{m+1} \\ a_{m+2} \\ \vdots \end{bmatrix} = 0$$

If interested states are edge states, then their energies will be strictly zero. Thus, linear combination of Bloch wavefunction components should add up to zero.

$$t(a_{m-1} + a_{m+1} + a_{m+2}) = 0 \tag{2.38}$$

By inserting Bloch wavefunctions to edge sites.

$$\begin{aligned} e^{ik(n)} + e^{ik(n+1)} + a_{n+2} &= 0 \\ a_{n+2} &= 2cos(k/2)e^{ik(n+1/2)} \end{aligned} \tag{2.39}$$

After applying the same procedure to next inner dimer, it can be found that density is proportional to $[2cos(k/2)]^2 m$, where m is the dimer number. Since zero energetic states are confined within $[\pi, 2\pi/3]$ region, a convergence condition $|(-2cos(k/2))| \leq 1$ should be introduced. This give rise to highly localized electron densities along the zigzag edges. On the other hand, more realistic spin dependent Hubbard model and DFT calculations predict that sublattice distortion should induce magnetism along the edges. This magnetism is ferromagnetic along the same edge however antiferromagnetically coupled with the opposite edge. This situation is in agreement with Lieb's theorem[25]. However, due to lack of control over edge geometry direct observation of edge magnetization is still lacking. Recently, at room temperature an indirect observation of magnetization has been done by studying the relation between energy gap and width of the ZGNR. In this study, it was concluded that ZGNR with energy gap corresponds to always antiferromagnetic (AFM) phase, however gapless structure experience a phase transition to ferromagnetic (FM) state. Difficulties of producing precise zigzag edges created a controversy among

scientist about whether it is possible to have these type of edges in real life. Some theoretical and experimental studies showed that zigzag edges experiences relaxation and forms (57) reconstructed edge geometry due to dangling bonds. However, in March 2016 a group successfully managed to fabricate long and narrow ZGNRs[28].

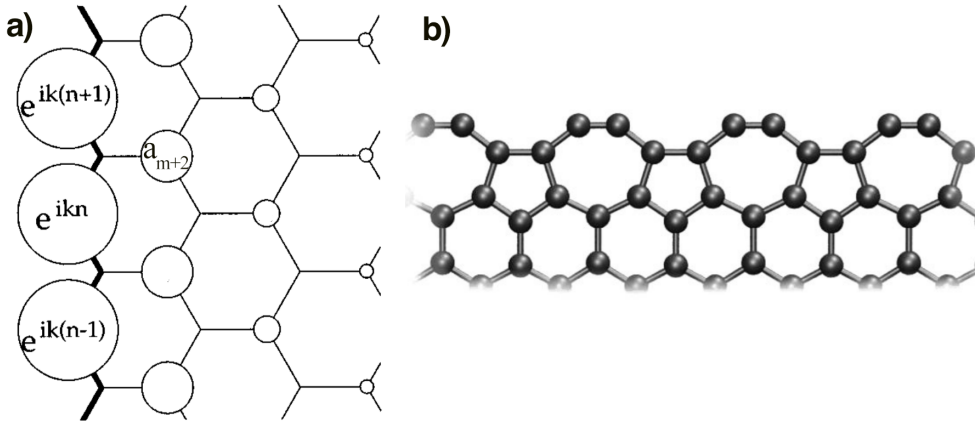

Figure 2.7. a) TB solution of edge states. Obtained from [19].b) Reconstructed (57) zigzag edges. Obtained from [34]

Armchair edges has protected sublattice symmetry and inverse proportionallity between energy gap and width. Due to sublattice symmetry, no zero energetic states and a distinct DOS peak around Fermi level is expected. Contrary to zigzag edges, nanostructures with armchair edges are more stable due to fabrication during aryl-arly coupling and produced for a long time [27].

Focus of this study is to investigate zigzag nanoribbons. No calculations are performed with armchair nanostructures.

2.3.2. Charged Impurities

A sheet of fabricated graphene is expected to have some number of foreign atoms which comes from either substrate or atmosphere. Therefore, even with a perfect honeycomb structure, absorption of different substances like hydrogenation of p_z orbitals can produce local potential hills or holes. It was shown both theoretically and experimentally that transport properties of graphene is highly dependent to these charged scattering sources. One of the most important anomaly induced by charged scatterers are the formation of inhomogeneous electron distribution so called ”electron-hole puddles”.

These highly inhomogeneous charge densities are detected experimentally by mapping the Fermi level. It was also shown electron hole puddles give rise to minimum conductivity of graphene due to ballistic transport between doping regions with different chemical potentials. Hence masks the phenomena known as Anderson localization type metal to insulator transition.

Modeling of the impurities is carried out with a superposition of Gaussian electrostatic potentials V_{imp}, which are randomly distributed over the sample.

$$V_{imp}(i) = \sum_{n} V_n \, e^{-\frac{(\vec{r}_i - \vec{r}_n)^2}{2\sigma^2}} \tag{2.40}$$

V_n is the potential peak value (randomly chosen between a minimum and a maximum value) of the n_{th} impurity located at $\vec{r}_n$, σ is the width of the potential.

To model smooth impurity potential landscape we take width of the impurity potential function as 10 times lattice constant of graphene. Figure 2.9 shows a randomly generated smooth impurity landscape.

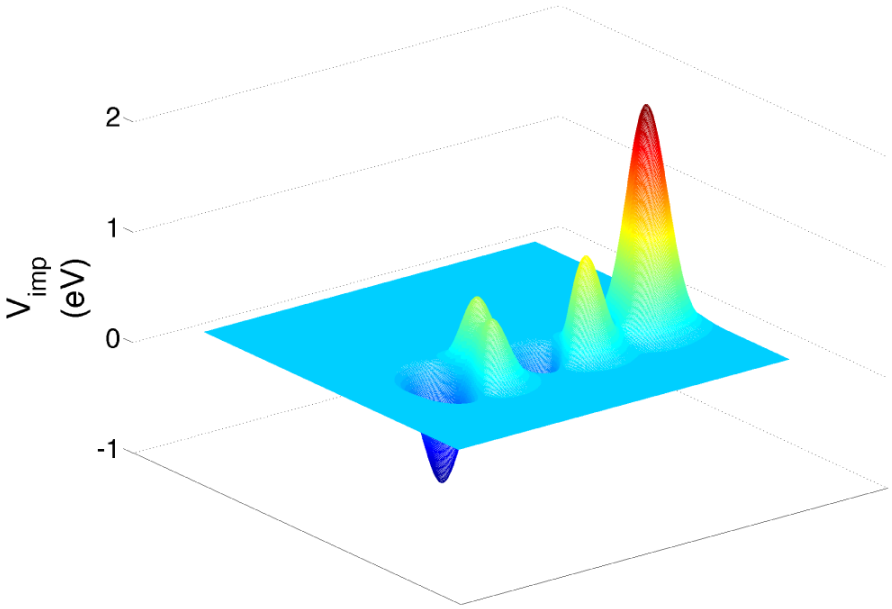

Figure 2.8. An example of randomly generated impurity landscape.

2.3.3. Adatom & Vacancy

Another charged scattering source is hydrogenated p_z orbitals. In their study Bostwick *et. al.* showed that 0.1% hydrogen coverage possibly disturbs transport of electrons in graphene by using angle-resolved photoemission spectroscopy (ARPES)[81]. Modeling of this type of impurities has been done by tuning the width of the impurity potential which is taken as 1% of the lattice constant. By doing this, we managed to break the sublattice symmetry and create possibility to induce backscattering. If geometric optimization due to dangling bonds are neglected, effect of a vacancy is similar hydrogenating of p_z orbital. One can model effect of vacancy by making Gaussian function very narrow and very high. However, vacancy type disorder is beyond the scope of this study.

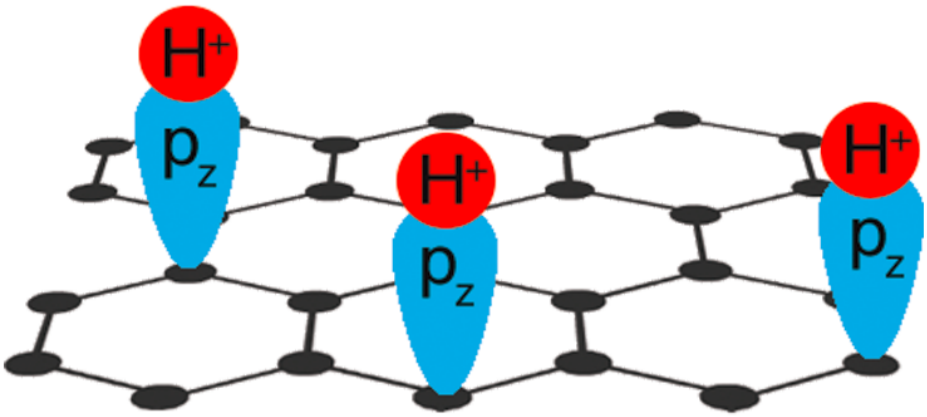

Figure 2.9. Hydrogeneation of p_z orbitals.

2.4. Anderson Localization

According the quantum mechanics, an eigenfunction of a disorder free system expands over all region. This property is in agreement with Einstein's diffusion equation that states random walk give rise to minimum conductivity[73]. However, in 1958 P. W. Anderson proposed that diffusion may come to an halt under impurity effects. He stated randomly distributed disorder within a region, if strong enough, may lead to localized wavefunctions[74]. These disorders can be charged impurities, filled orbitals, vacancies or any deviation from perfect crystal lattice. A localized wavefunction can be formulated

as,

$$\Phi = e^{-r/\lambda} \sum_i A_i \phi_i(\vec{r} - \vec{r}_i) \tag{2.41}$$

where summation i is over all sites and r_i denotes site location. Exponential decay term gives information about localization length λ which is a finite quantity if the wave is localized. In non-localized state wavefunction is extended and λ goes to infinity which corresponds to Bloch wavefunctions. At finite temperatures transport occurs due to thermal excitations and Coulomb repulsion. However, at $T = 0K$ when phonon vibrations are neglected, only extended states contribute to conductivity. Wavefunctions with finite λ values are localized. Therefore they do not transport any charge. In his original work, Anderson proposed that every lattice site has some amount of random impurity potential. If this value is strong enough at $T = 0K$ conductivity vanishes and system becomes insulator. This phenomena is called the Anderson Localization[74]. Later, Anderson's pure mathematical idea is applied to condensed matter system by Nevill Mott, John van Vleck and Thouless after introduction of the scaling idea[75, 76]. Inspired by the Schuster's paper[77], Anderson, Licciardello, Ramakrishnan and Abrahams applied the scaling idea to statistical mechanics and showed metal-insulator transition with vanishing conductivity[78]. Following this paper, effect of spin-orbit coupling, magnetic impurities, inelastic scattering and effect of magnetic field are investigated [79, 80].

One could formulate this system by defining the following Hamiltonian,

$$H = -t \sum_{<i,j>} (c_i^\dagger c_j + c_j^\dagger c_i) + \sum_i V_i c_i^\dagger c_i \tag{2.42}$$

where first summation is earlier TB and second summation represents on-site impurity potentials.

On the other hand, discovery of graphene provided a new playground for scientist who work on Anderson localization[83–86], since graphene is expected to have minimum conductivity. Hydrogen atoms tend to create bonds with p_z orbitals of graphene. From theoretical point of view, hydrogenation directly corresponds to impurity contributions to diagonal terms. This phenomena first showed in graphene by 0.1% hydrogen coverage[81]. However, experimental evidence of Anderson localization is still lacking. Because local chemical potential differences lead to ballistic transport between electron-hole puddles. It was shown that, if the formation of these charge inhomogeneities are suppressed, resistivity increases rapidly when thermal excitation effects are reduced[82]. One of the other significant property graphene has is the absence of backscattering. If the

disorder affects long range, then sublatice symmetry is conserved within perturbative limits and leads to intervalley scattering. This symmetry give rise to destructive interference of scattered waves. Thus transport is always along the incident direction and conductivity never reaches to zero. On the one hand, hydrogenation of graphene does not conserve the sublattice symmetry, due to intravalley scattering. So, backscattering should be observed and if the impurities are strong enough, localized wavefunctions should be observed[87].

2.5. Optical Conductance of Graphene

On the other hand, optical properties of graphene as well can be explained within Dirac approximation. It was observed that absorption of single layer graphene is strictly equal to fine structure constant. Hence, it is an intrinsic property without material dependence. Study of Ref. [47] also shown that number of layers of graphene is linearly proportional to absorption of graphene. One of the most important consequence of this property is that a fundamental quantum mechanical constant can be probed only by shining light on to graphene sample. Optical conductivity of graphene is dominated by two different mechanisms; intraband and interband optical transitions, according to interested energy region. Intraband transitions take place far-infrared region where carriers are mostly free. Theoretically this region can be explained within Drude model[71]. In near-infrared to ultraviolet region however, excitations are dominated by interband transitions which arises from electron transfer from valence to conduction band. Frequencies higher that far-infrared region corresponds to optical conductivity of graphene which is proportional to fine structure constant. It was found that around K and K' point where linear dispersion prevails, optical characteristics are frequency independent. Within this model by doping the sample, it is possible to shift the Fermi level and change the optical characteristics by exploiting Pauli blocking. In this study we only consider interband transition and neglect transition that can be explained within Drude model. Figure 2.10 shows the pictorial representation of interband transition and Fermi level shift due to hole doping.

$$\sigma(w) = \pi e^2/2h, A(w) = 4\pi\sigma(w)/c \approx 2.3\% \tag{2.43}$$

where α is fine structure constant.

We are going to begin theoretical description first by assuming reflection of graphene is very small (0.1%) hence it can be neglected.

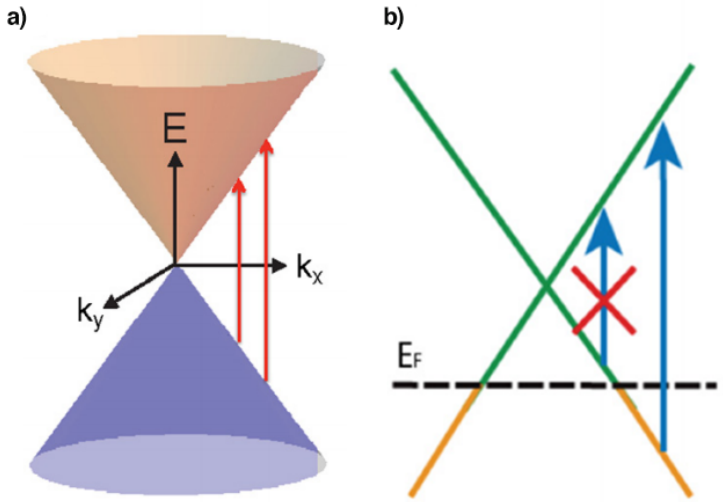

Figure 2.10. a) Interband optical transitions.(b) Fermi level shift due to hole doping and Pauli blockade. Obtained from Ref.[70]

$$A \approx 1 - T \tag{2.44}$$

Now within time dependent perturbation theory, interaction of system with electromagnetic field can be given with Coulomb gauge.

$$H = \frac{p^2}{2m} + e\psi(x)\frac{e}{m}\vec{A}\cdot p \tag{2.45}$$

where $\vec{A}$ is vector potential which is harmonic and can be written as,

$$\vec{A}(\vec{x},t) = A_0\hat{\epsilon}[e^{i(\vec{k}\cdot\vec{x}-wt)} + e^{-i(\vec{k}\cdot\vec{x}+wt)}] \tag{2.46}$$

where first exponential term corresponds to stimulated emission and later is absorption. Now by using Fermi's golden rule[88]

$$w_{i,n} = \frac{2\pi}{\hbar}(V_{i,n})^2\delta(E_n - E_i) \tag{2.47}$$

where

$$V_{i,n} = -\frac{eA_0}{m}(e^{i\vec{k}\cdot\vec{x}}\vec{\epsilon}\cdot\vec{p}) \tag{2.48}$$

Insert this into Fermi golden rule,

$$w_{i,n} = \frac{2\pi}{\hbar}\frac{e^2}{m^2}A_0^2 \langle n| e^{i\vec{k}\cdot\vec{x}}\vec{\epsilon}\cdot\vec{p}\,|i\rangle\, \delta(E_n - E_i - \hbar w) \tag{2.49}$$

Now, absorption cross section can be defined as,

$$\sigma = \frac{\text{Energy absorbed in unit time}}{\text{Energy flux of the field}} \tag{2.50}$$

Using following Maxwell equations,

$$E = \frac{\partial}{\partial t}\vec{A}(\vec{x},t), B = \nabla \times \vec{A} \tag{2.51}$$

energy flux can be written as,

$$U = \frac{w^2}{2\pi}A_0^2 \tag{2.52}$$

Thus absorption cross section becomes,

$$\sigma = \frac{4\pi^2\hbar}{m^2 w}\underbrace{\frac{e^2}{\hbar c}}_{\alpha=1/137} |\langle n| e^{i\vec{k}\cdot\vec{x}}\vec{\epsilon}\cdot\vec{p}\,|i\rangle\,|^2\delta(E_n - E_i - \hbar w) \tag{2.53}$$

Since absorbed the wavelength of electromagnetic wave that cause electron excitation is more bigger than radius of carbon atom, we can use electric dipole approximation as follows,

$$e^{i\vec{k}\cdot\vec{x}} = 1 + \cancelto{0}{ik\vec{x} + \ldots} \tag{2.54}$$

and switching from x to p by using,

$$[x, H_0] = \frac{i\hbar\vec{p}}{m} \tag{2.55}$$

which gives,

$$\langle n|\,\vec{p}\,|i\rangle = imw_{ni}\langle n|\,x\,|i\rangle \tag{2.56}$$

where $\langle n|\,\vec{x}\,|i\rangle$ dipole moment between i and n sites. Finally absorption cross section

becomes,

$$\sigma(\omega) = 4\pi^2 \alpha w_{ni} |\langle n| x |i\rangle|^2 \delta(E_n - E_i - \hbar w) \tag{2.57}$$

CHAPTER 3

RESULTS AND DISCUSSIONS

Before discussing the results, some calculation details should be given. For all calculations both for TB and MFH hopping parameters are taken as $t_{nn} = -2.8eV$ for nearest neighbors and $t_{nnn} = -0.1eV$ for the next-nearest neighbors[9]. On site Coulomb interaction term U is taken to be $16.522/\kappa$ where κ is effective dielectric constant taken to be as a control parameter. This value of the integral shown in Eq. 2.24. For the long-range off-site Coulomb interactions V_{ij} are taken as $8.64/\kappa$ and 5.53κ for neighbors and $1/d_{ij}$ for other distant atoms. These values correspond to integral in Eq. 2.26. All interaction integrals are calculated using Slater π_z orbitals [72]. For long range impurity potential sixteen, for short range about two percent scattering regions are used. MFH problems are solved self consistently. To find the ground state magnetic phase, all spectrum within $S_z = 0$ and $S_z = 35$ is scanned for not to miss any other magnetic phases. To be certain, some calculations are repeated beyond that region, although they are not presented in this work.

3.1. Long Range Disorders

First structure we have investigated is the finite one with no periodic boundary conditions applied which is 5.83 nm wide, 25.5 nm long and consists around 5800 carbon atoms. ZGNR with this length give rise to approximately 60 edge states. Figure 3.1(a) shows the topical structure of this section. Calculations started within TB model then obtained electron densities and energy spectrum. But, since it has no spin dependence, TB model gives no information about spin polarized edges and magnetism.

3.1.1. Electronic Properties

Figure 3.2 shows the electron density profile of edge states where first row (second row) calculated within TB (MFH) model for the impurity configuration in Figure 3.1(b). Columns, on the other hand, indicate how many states are taken into account for density profile calculations. There are two conclusions we can make from Figure 3.2. First,

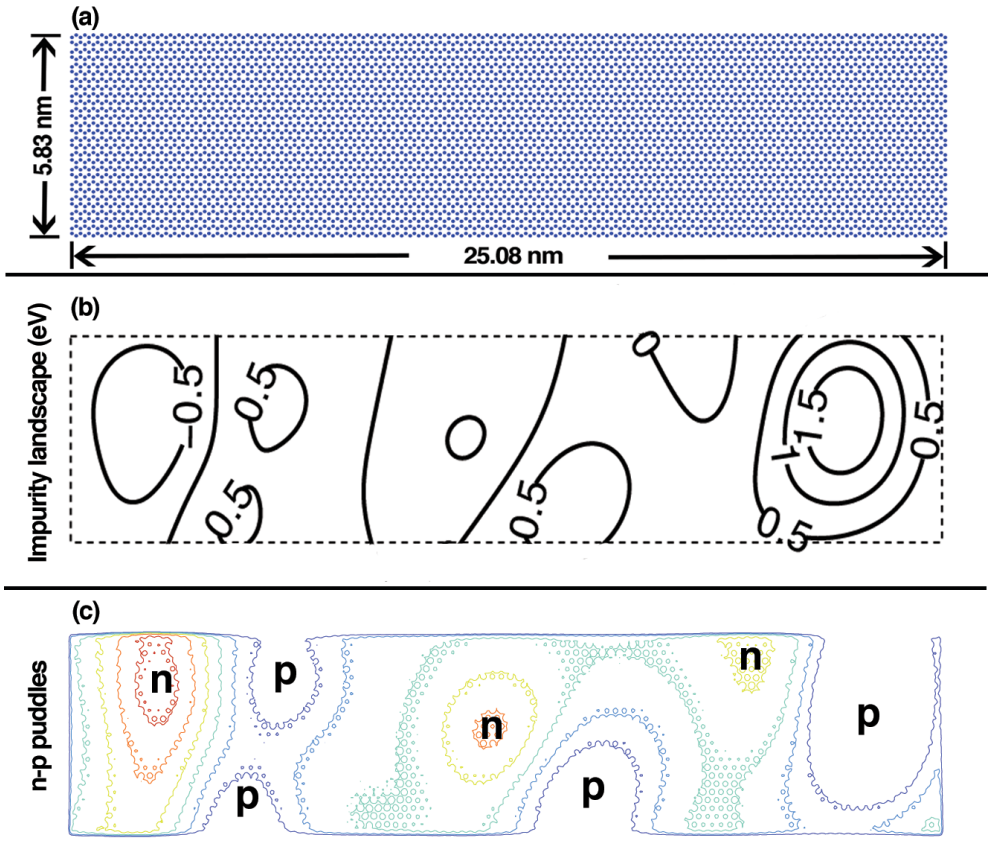

Figure 3.1. (a) Graphene nanoribbon lattice structure. (b) Randomly generated impurity potential landscape. (c) Total electron density showing the formation of electron-hole puddles (regions denoted by n and p), obtained from mean-field Hubbard calculations.

comparing the TB and MFH results, edge densities are more scattered within TB model. However, including the electronic interaction effects make edge states robust against the same impurity configuration. Second inference is, clean system edge state contribution only comes from the most energetic valence states, but introducing the scattering sources to system breaks this rule. While for clean sample first 30 states contribute to the edge densities, for disordered system, edge states spreads deep into bulk states. This time highest energetic 60 valence states gives contribution edges. By looking at the (b) and (c) plots of this figure, a question rises. Why electrons do not fill the p regions that can be seen in Figure 3.1(c) while they accumulated in these regions within Hubbard model? At the first glance this looks like a discrepancy, however one should remember that Hubbard calculations give more realistic spin-dependent filling of the states. Magnetic dipole moments along the edges in disorder system is consistent with earlier theoretical work[38]. Therefore this anomaly can be explained as a shortcoming of TB compared to Hubbard model.

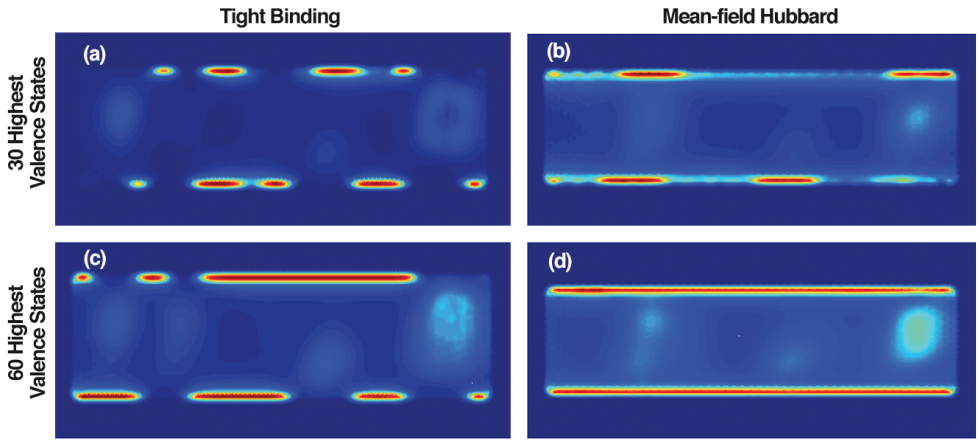

Figure 3.2. Electronic density profile corresponding to the 30 highest occupied valence states (top panels), and the 60 highest occupied valence states (bottom panels), obtained using tight-binding (left panels) and mean-field Hubbard calculations (right panels). Electron-electron interactions restore the edge states.

Similar to earlier figure, density of states (DOS) analysis shows more delocalized states for TB(Figure 3.3) method and there is a considerable amount of difference between clean and disordered system. But MFH(Figure 3.4) densities are more similar to clean DOS. Peaks around 0 eV is due to edge states and in agreement with earlier studies [59]. Since there is no spin polarization on TB, single peak appears. However, when spin is

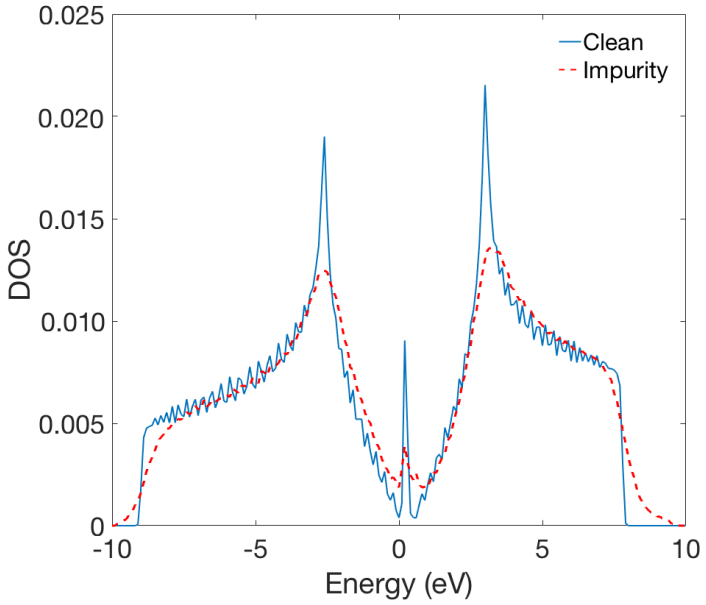

Figure 3.3. TB DOS of finite ZGNR. Peak around Fermi level is due to edge states.

included two peaks with different spin orientation appear around Fermi level.

3.1.2. Magnetic Properties

Now another question arises, how the magnetic properties of the system affected by the combined effect of disorder and electron-electron interaction, which we are going the focus rest of this section. Figure 3.5 shows the band structure the sample for various impurity strengths. First row is for antiferromagnetic(AFM) phase which has equal number of up and down electrons. Second row consists belongs to ferromagnetic(FM) phase where $n_{up} - n_{down} =$ Number of Edge States. By doing this we managed to create same spin orientation along the both edges. Columns, on the other hand, plotted with respect to disorder strength. When there is no scattering sources, ground state configuration is AFM and a 0.17 eV gap appeared in agreement with previous theoretical and experimental studies [18, 20, 23, 68]. Introducing the disorder, weak impurity reduces the AFM energy gap to 0.1 eV. But no phase transition is observed. However by looking at to the last column of Figure 3.5, doubling the impurity height, causes system to undergo a phase transition from AFM to FM. At this point the ground state is FM configuration and one can see that AFM gap is vanished in agreement with [20], where value of the energy gap

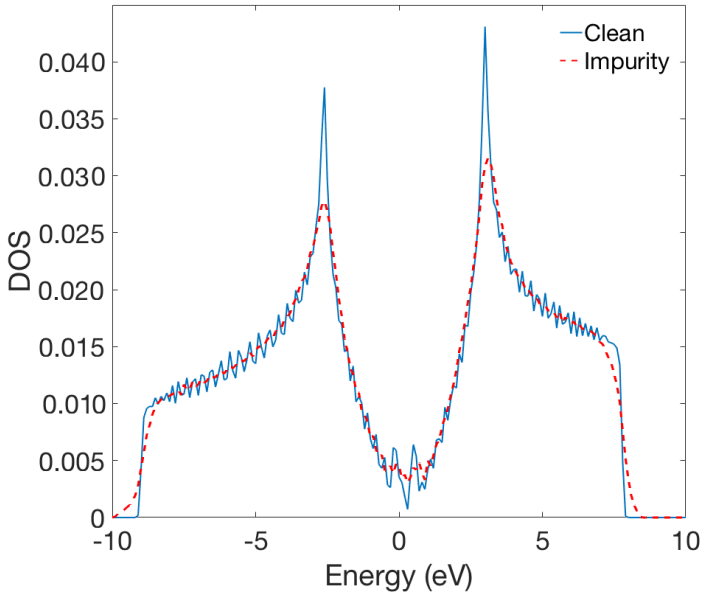

Figure 3.4. MFH DOS of finite ZGNR. Sharp edge state peak at preceding figure is now spin polarized.

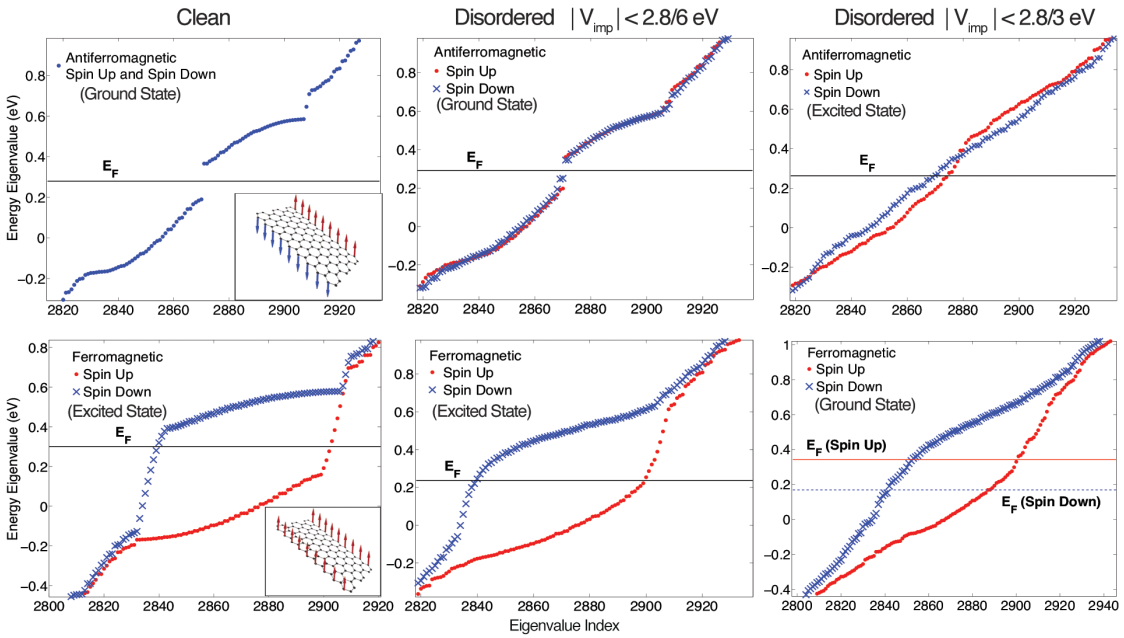

Figure 3.5. Mean-field Hubbard spectra for antiferromagnetic (top panels) and ferromagnetic (bottom panels) phases, for various degrees of disorder strengths, characterized by V_{imp}. E_F spin up and spin down show the spin-dependent Fermi levels.

is investigated with respect to width of the ribbon. They found that ZGNR whose width exceeding the 7 nm are always in FM phase. But in this work, without changing the width of the ZGNR, we showed that is possible to observe AFM-FM phase transition. Results of figure 3.2 and 3.5 are for the same impurity locations but with different strengths. In order to be certain about observation of phase transition, we repeated the same calculation 30 times for different impurity configurations and strengths. Results are reported in figure 3.6 where (a) subfigure shows the AFM-FM energy difference per atom. A negative value there indicates AFM phase, otherwise system is FM. For low impurity strength, no phase transition is observed, but increasing the impurity height leads gradual increase in transition chance. In the end for very strong impurities, 9 out of 10 samples experienced AFM-FM phase transition. Subfigure below shows the corresponding AFM energy gaps of these runs. It can be concluded that, AFM gap vanishes rapidly by increasing the impurity strength and becomes negligible for strong disorders. As it was stated above AFM phase corresponds to $S_z = 0$ and the FM phase $S_z = 32$. To be certain about any other magnetic phases are not missed, we performed calculations with the same impurity configuration but with different S_z values in the range between 0 to 35. Figure 3.7 shows result of these calculations. Confirming the earlier results, $S_z = 32$ (FM) phase has the global minimum energy. It is also clear that no other magnetic phases appeared within this limit. Thus it was concluded that extended Hubbard model is dominated by two phases; AFM and FM for ZGNRs.

In our calculations there are three main variables, hopping parameter t, impurity strength and electronic interaction strength. In all preceding calculations only impurity strength and configuration is varied. Its beneficial to see the effect of electronic interaction strength on earlier results. One can tune this value by changing dielectric constant κ whose value directly affects U and V_{ij} terms. To see the correlation between κ and magnetism same calculations are performed within $1/\kappa = [0.3, 0.002]$ range. Since summing up the magnetic moments of the electrons gives no information about how magnetism changes, it is convenient to use staggered magnetism to investigate staggered magnetism which is defined as $\sum_i (-1)^x (n_{i\uparrow} - n_{i\downarrow})/2$ where x is even for A and odd for B sublattices. Figure 3.8 shows the value of the staggered magnetism as a function of $1/\kappa$. For clean system, as expected, AFM phase is covered in this region but value decreases as electronic interaction loses its strength (gets closer to TB model). Another confirming result can be inferred from impurity curve. System is FM between $1/\kappa = [0.167, 0.04]$ however becomes AFM again $1/\kappa$ values greater than 0.167. This results are again consistent with ours. As electron-electron interaction strength increases, effect of impurities

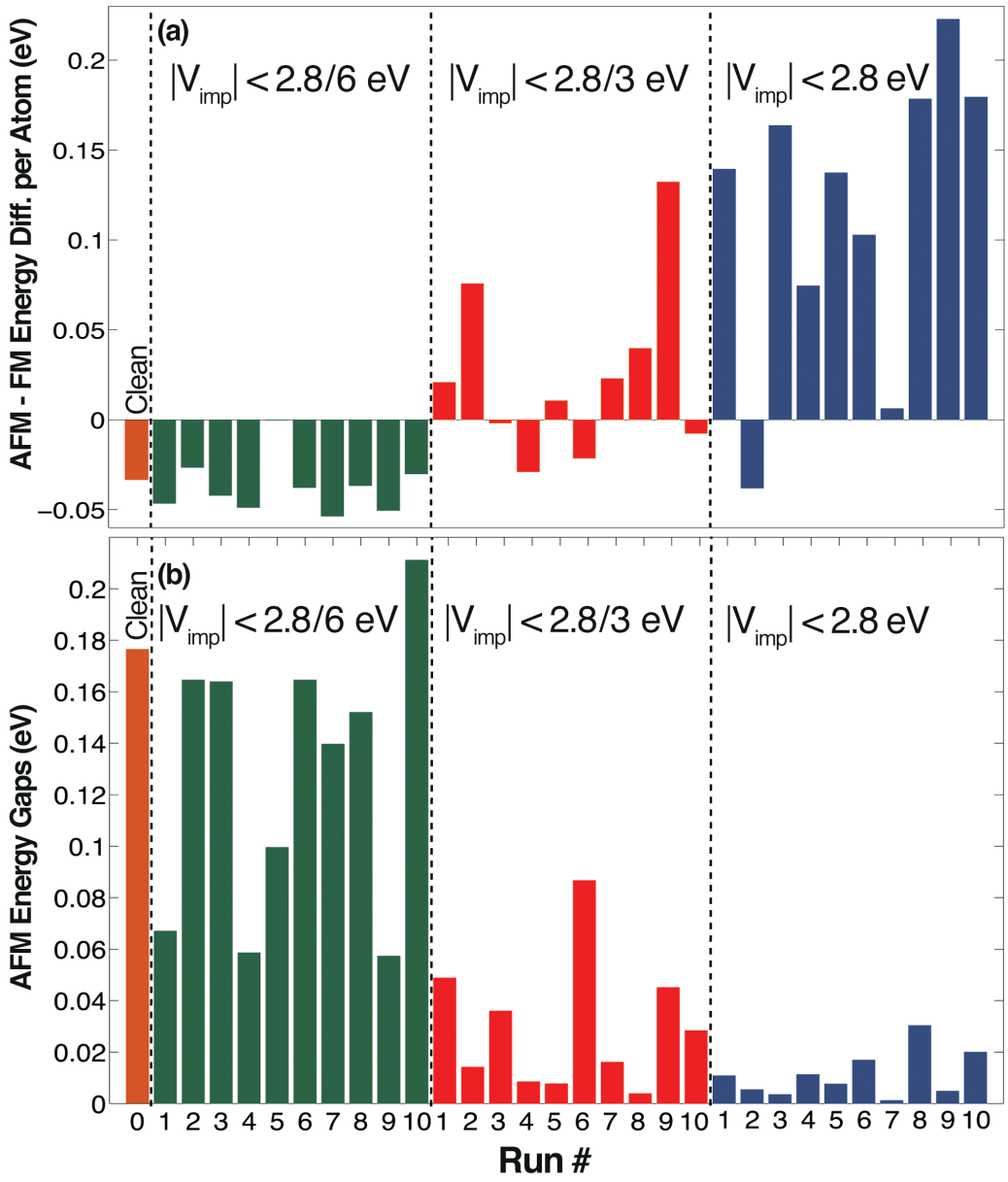

Figure 3.6. (a)Energy difference per atom between the AFM and FM phases and (b) the antiferromagnetic phase energy gap for 30 different disorder configurations with various degrees of disorder strengths. A strong disorder effect causes the system to become ferromagnetic. For lower potentials, the chance of a phase transition reduces.

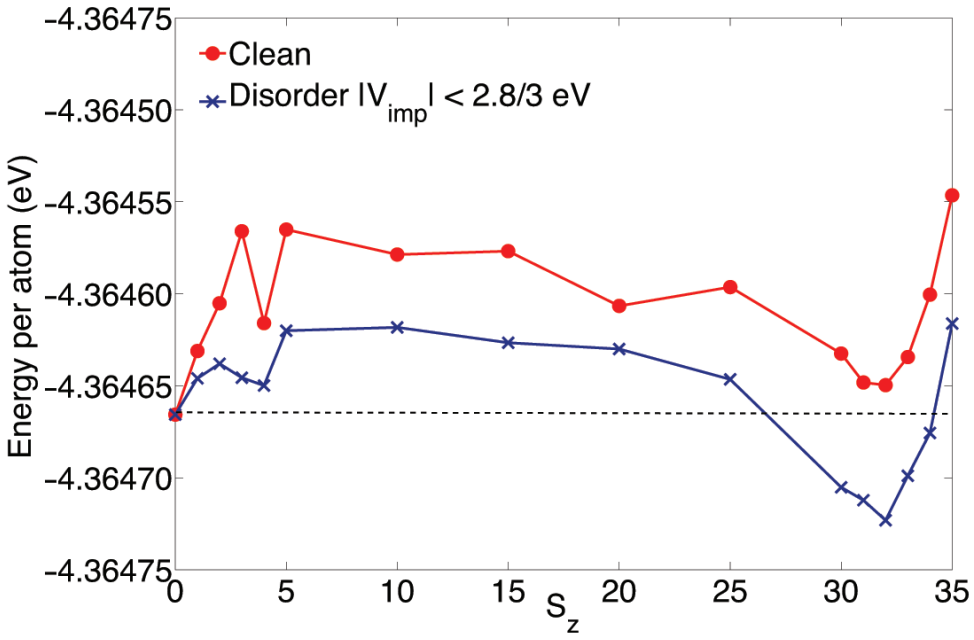

Figure 3.7. Total energy of a nanoribbon as a function of magnetization S_z. For the clean case, the ground state has $S_z = 0$, and for the disordered case $S_z = 32$, indicating a FM-AFM phase transition without involving other possible magnetic phases.

are suppressed thus system becomes AFM. But for smaller κ values, impurities become dominant and phase transition occurs. For small κ values magnetic properties can be neglected.

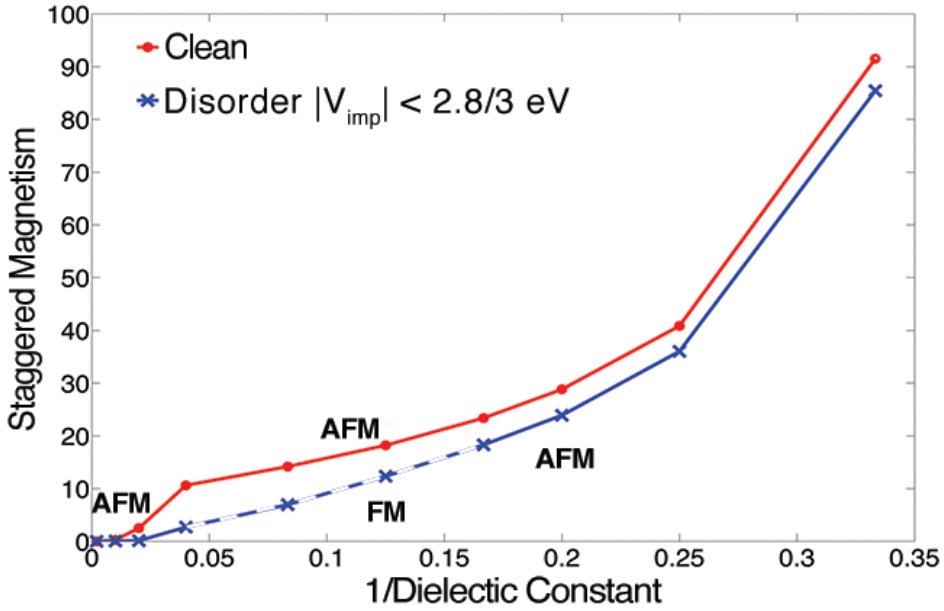

Figure 3.8. Staggered magnetism as a function of dielectric constant κ. The clean system (upper line) shows AFM (solid line) coupled edges for all values within the $1/\kappa$ = [0.33,0.002] range. However, a FM (dashed line) phase transition occurs between $1/\kappa$ = [0.167,0.04] after introducing the impurity landscape (lower line). For lower κ values, electronic interaction effects become dominant over the impurities hence the system shows an AFM phase again.

3.1.3. Optical Properties

So far, correlation between electronic and magnetic properties are covered. In this part, relation between magnetic and optical properties will be investigated. Through out this section, incident light will be divided into two perpendicular components, X where quantum confinement is dominant and Y direction where system shows bulk like behavior.

Discussion begins with polarization along Y-direction where quantum confinement effect is minimum. By comparing the clean and disordered system, it was observed that tight binding model gives a sharp peak near Fermi level. However, as it confirms the

earlier results, electronic interaction effects reduces the impurity effects, lowers the peak and recovers the clean nanoribbon properties.

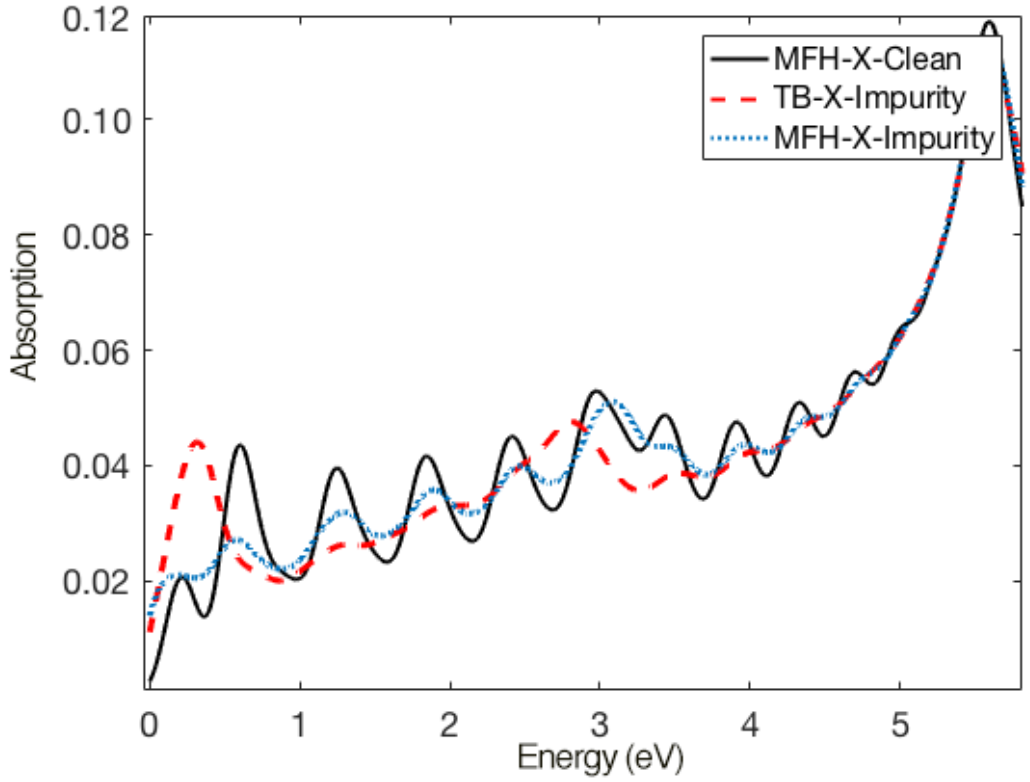

Figure 3.9. Comparison of pure MFH (solid black), disordered TB(dashed red), disordered MFH (dotted blue) absorption spectra. Within TB model, a peak induced.However, electronic interaction effects help system to recover its pure-like state.

Next, for the X-polarized light whose low energetic absorption characteristics are mostly determined by quantum confinement and edge effects, clean and impurity comparison is shown in Figure 3.9. Similar to Y-polarized result, effect of disorders washed out by electronic interaction. It is also remarked that, oscillations between 0-5 eV are due discreteness of energy levels which induced by quantum confinement. Since the impurity disrupts this feature, energy levels become more bulk like continuous. Bump around 3.0 eV are due to edge states.

Another analyze we will perform is whether there is an optical absorption characteristics difference between AFM and FM phase due to Fermi level shift and Pauli blocking. For Y polarized light, shown in Figure. 3.10 high energetic transitions are exactly the same. However, around Fermi level a small peak appears in FM phase. The same

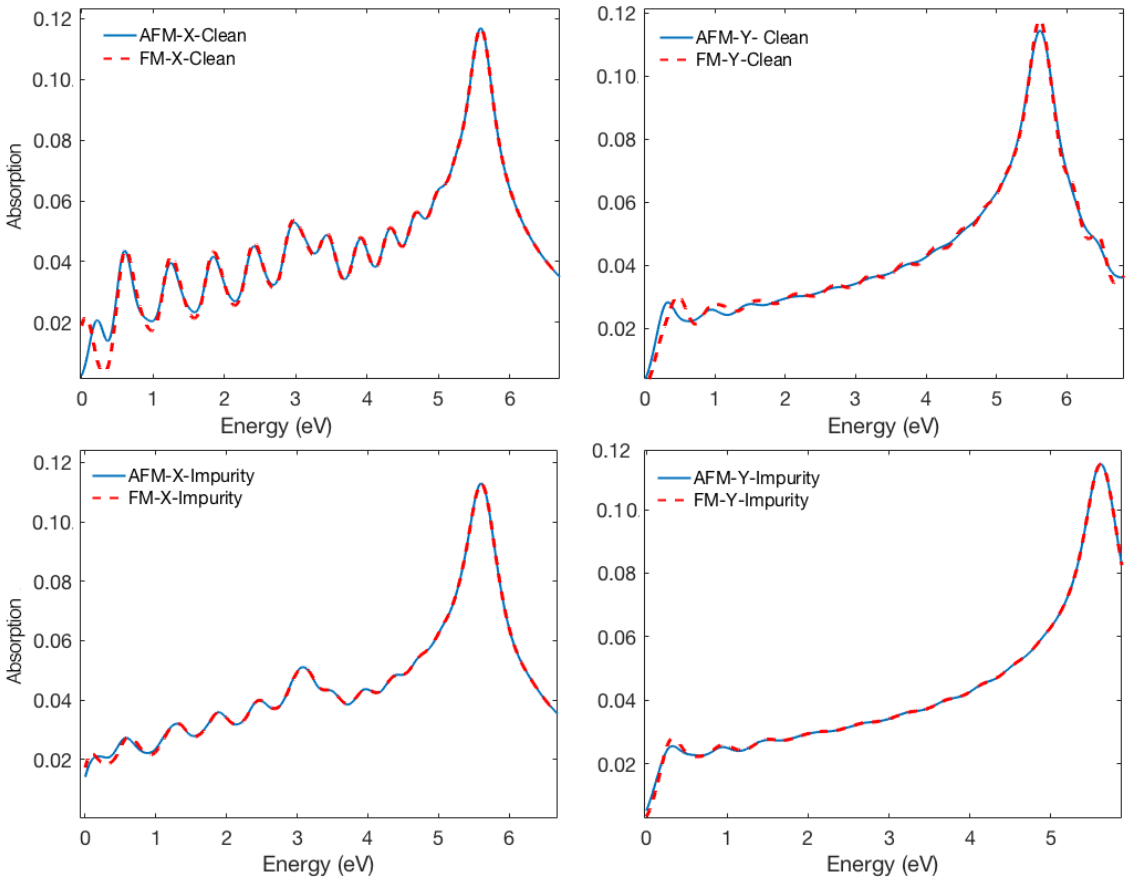

Figure 3.10. Comparison of pure MFH (solid black), disordered TB(dashed red), disordered MFH (dotted blue) absorption spectra. Within TB model, a peak induced.However, electronic interaction effects help system to recover its pure-like state.

peak appeared for X polarized light as well, but this time with higher value. Since it is stronger in X-polarized absorption spectrum, we made a deep level investigation. Figure 3.11 shows the absorption between 0-5 eV. As shown in the figure, FM phase peak almost doubles the AFM peak around Fermi level. Although these two peaks around the same energy their cause is completely difference. By investigating the which dipole moment between states causes these peaks, it was determined that interaction between edge states give rise to AFM peak. On the other hand, FM peak is induced by interaction between two edge-bulk transition states. Interaction between two opposite edges are small compared to interaction between bulk and edge since overlap between are neglible. Because of interaction strength, FM phase absoption probability is almost double of the AFM phase at that energy level.This interactions explains the magnitude difference between peaks as well. Since electron at an edge site only jump to opposite edge sites which has small overlap with, absorption probability is 1%. But in FM phase edge and bulk interacts more easily and resultant peak is double of the AFM peak. The peak height difference between X $\&$ Y polarized light is due to dominance of quantum confinement in the former one.

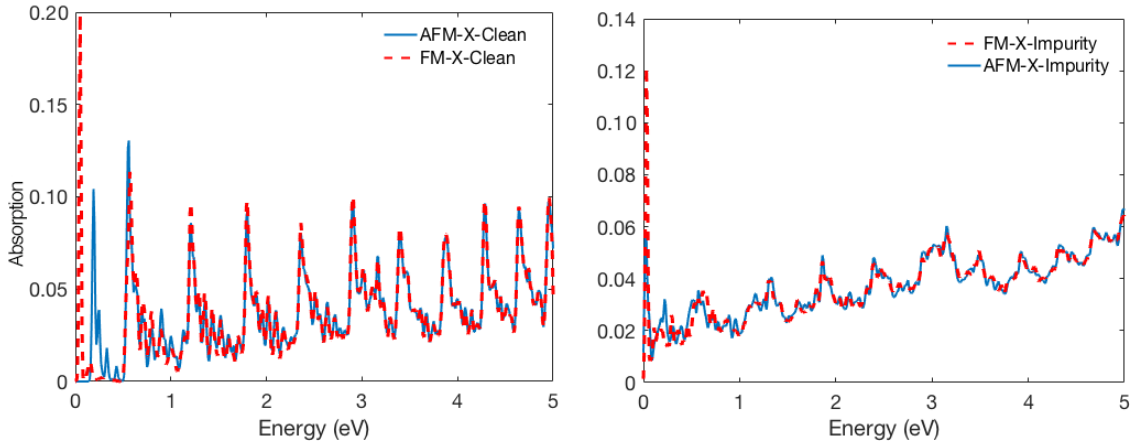

Figure 3.11. Comparison of pure MFH (solid black), disordered TB(dashed red), disordered MFH (dotted blue) absorption spectra. Within TB model, a peak induced.However, electronic interaction effects help system to recover its pure-like state.

In conclusion, it was proposed that by looking at the absorption characteristics magnetic phase of the graphene nanoribbon can be determined with a linearly polarized light. This possible characterization property is observed both in clean and disordered system. However, since observed peak is located around Fermi level where our mean field model does not work properly, this behavior should be investigated within models

those take electron correlation more precisely take into account.

3.1.4. Cyclic Zigzag Graphene Nanoribbon

In this section subject is a nanoribbon in cyclic topology which was constructed by applying periodic boundary conditions to finite system investigated above. This structure has 5712 atoms due to topological constraints but has the same number of edge states. It should also be noted that, same impurity configuration shown in Figure 3.1 is used with periodic boundary conditions applied.

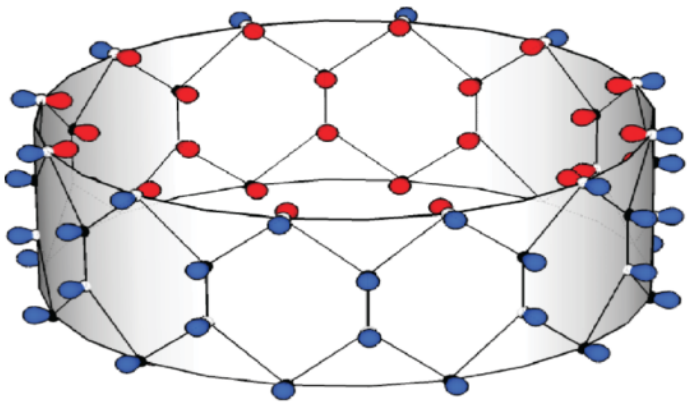

Figure 3.12. Topology of the cyclic nanoribbon

Figure 3.13 shows the electronic density profile of the cyclic structure. Similar to finite nanoribbon edge state densities, disorders within TB model disrupts the edge states and make them localized around the scattering sources. But, electronic interaction recovers the edge states. In addition to that, spreading of the edge states into deeper states again visible. However, no correlation have been found between electronic interaction and magnitude of state spreading. Filling of the n doped regions with electrons also removed by introducing more realistic spin filling system. 2nd column of Figure 3.18 shows the correct filling of the electrons into p regions. Now, the electronic structure investigation is finished, it is beneficial to take a close look to correlation between electronic and magnetic properties. Figure 3.14 shows the AFM and FM(rows) phase band structure of clean and disordered (columns) cyclic nanoribbons. Similar to finite structure, energy gap disappears after introducing the strong enough impurity. Also phase transition occurs. It

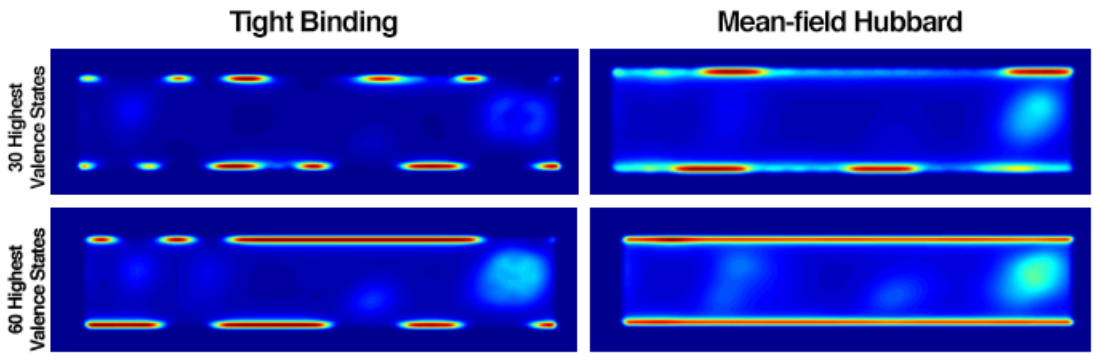

Figure 3.13. Similar to finite structure results; while TB mode gives highly localized edge states, electronic interaction recovers the edge states. Spreading of the edge states is also visible by comparing the columns.

is also noted that, energy levels are now doubly degenerate which is due to angular momentum parity. For clean system, ground state is in AFM phase. But disorders cause system to undergoes phase transition to FM. Scanning between $S_z = 0$ and $S_z = 35$ is also performed. Figure 3.15 gives information about this calculation. Since number of edge states is the same with the finite sample, ground state of the disordered cyclic system is $S_z = 32$ which is FM phase basically.

Our optical absorption model only considers perpendicular incident light. However, in cyclic case light never does so, since ring form has curved shape. Except, polarized light along finite direction which is always normal to the surface. But, due to same topology, absorption characteristics along Y-direction for finite and cyclic nanoribbons are exactly the same thus results do not introduce any new data.

In conclusion, this section is devoted to cyclic graphene nanoribbon. There, we have showed, similar to finite sample, electronic interaction recovers the disrupted edge states under potential fluctuations and magnetic phase transition from AFM to FM state occurred. Main difference between two samples appeared in band structure where cyclic system showed doubly degenerate level with greater energy gap.

To sum up, by using finite and cyclic nanoribbon we first showed that electronic interaction effects recover the edge states electronic density profile. Then, by using these results a magnetic phase transition from AFM to FM state is observed. This observations has been associated to electronic energy band profile, while AFM state has a band gap, FM has no such forbidden region. We verified this result by different disorder configurations and strengths. Finally, a relation between magnetic and optical behavior has been set up

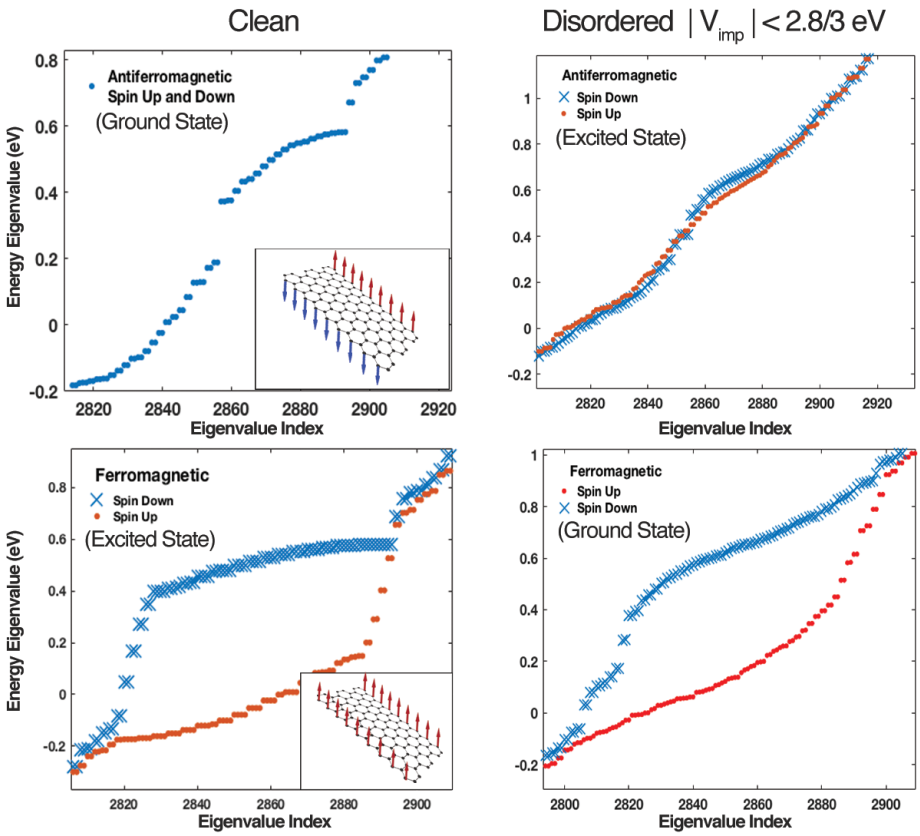

Figure 3.14. In cyclic topology, mean-field Hubbard spectra for antiferromagnetic (top panels) and ferromagnetic (bottom panels) phases, for various degrees of disorder strengths, characterized by V_{imp}. It must be noted that levels are doubly degenerate in this type of geometry.

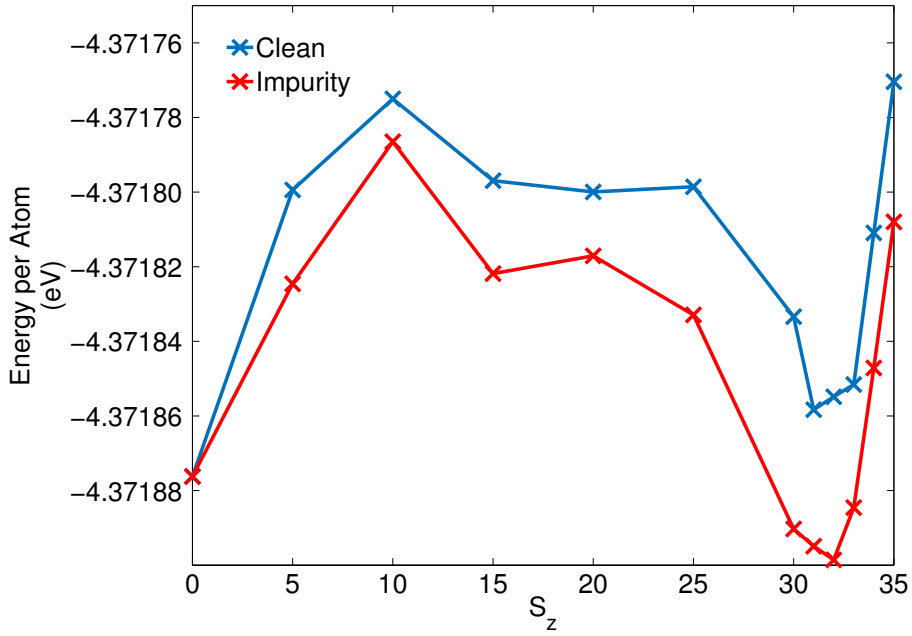

Figure 3.15. Energy per atom a cyclic nanoribbon as a function of magnetization S_z. Similar to finite structure, for the clean case, the ground state has $S_z = 0$, and for the disordered case $S_z = 32$. There are no other dominant magnetic phases could be found.

where a low energy peak can be used to distinguish FM phase from AFM phase.

3.2. Short Range Disorder

Up to now, impurities are modeled with Gaussian function whose width is 10 lattice constant. However, to investigate the effect short range disorders, width of the Gaussian is reduced to 1% of the lattice constant to create a Dirac delta like behavior. The maximum height of the disorder function is increased to $6t$. For this part a longer (55.5 nm) and thinner (4.5) structure is generated in order to observe localized electron waves easily. For all calculations 2% impurity density and the same impurity locations are used. Figure 3.16 shows the structure and impurity distribution over the sample. Electron waves started to diffuse through the ribbon from the lead part, where there is no impurity effect is taken into account.

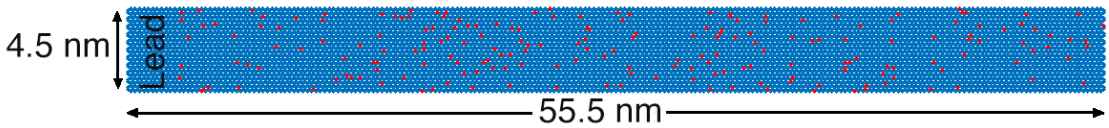

Figure 3.16. Structure and impurity distribution used for Anderson localization calculations. Red dots represent hydrogenated p_z orbitals.

3.2.1. Time Independent TB Solution

Figure 3.17 compares the clean and disordered DOS for this system. Bump around -0.5 eV are due to accumulation of impurity states at that region. Since these hydrogenated orbitals tend to pile up in a domain, not homogeneously dissipate through whole spectrum, it is convenient to investigate this structure by dividing into four parts. Fig 3.18 shows puddle formation within this four regions. Dotted structure in second region shows the impurity states accumulated there.

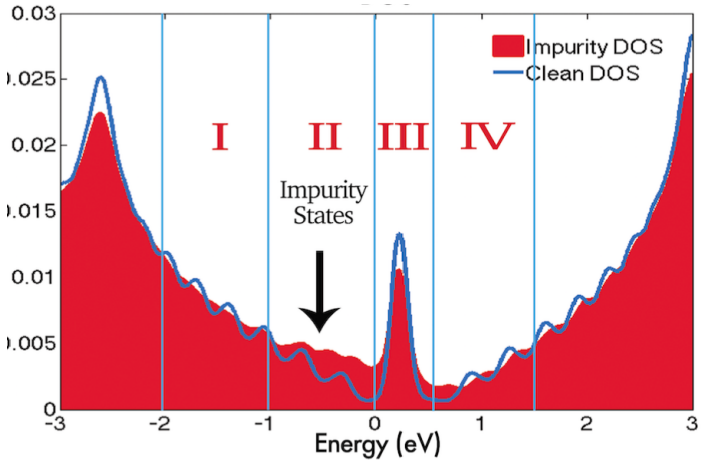

Figure 3.17. Blue line represents clean and red area shows disordered DOS. Since impurities do not homogeneously dispersed, area by area investigation is required

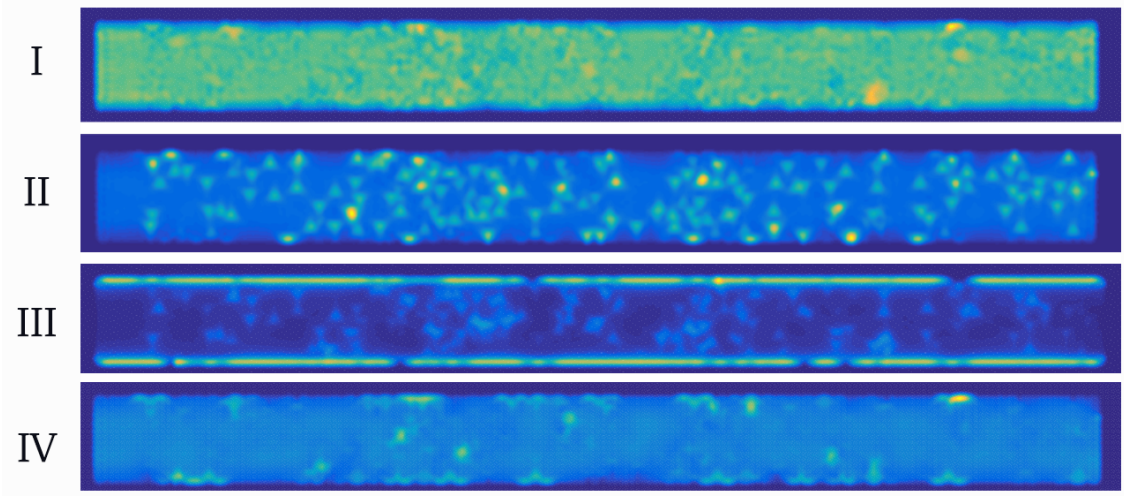

Figure 3.18. Puddles formation within four regions in Figure 3.10

3.2.2. Time Dependent TB Solution

In this section we solved time dependent Schrödinger equation to investigate diffuse of the wavefunction through clean and disordered nanoribbons. Starting from time dependent wavefunction equation,

$$|\Psi(t)\rangle = \sum_n C_n \, |\psi_n\rangle \, e^{\frac{-iE_n t}{\hbar}} \tag{3.1}$$

One can obtain C_n by taking $t = 0$ and by choosing any initial wavefunction $\Psi(0)$.

$$\langle \psi_n | \Psi(0) \rangle = C_n \, \langle \psi_n | \psi_n \rangle \tag{3.2}$$

First region in Figure 3.17 is the deepest valence state that will be considered. Within this region, some charge inhomogeneities is observed and some impurity states also included. An incident wave with energy -1.55 eV which corresponds to an eigenvalue within this region, diffuse through ribbon in Figure 3.12. Wave is not localized, some fraction of it reaches to the right side. Hence, it can be inferred that transport is not deteriorated in here. In second region of Figure 3.10, impurity states can be found.

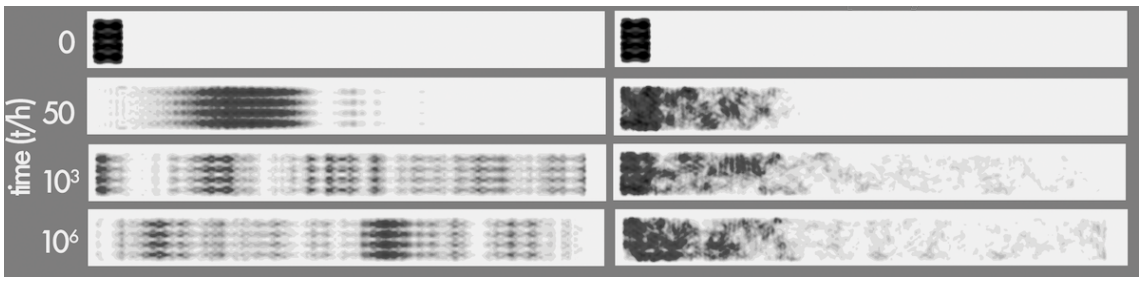

Figure 3.19. Clean (left) and disordered (right) time dependent solution of wave function dispersion within first region with incident particle energy -1.55 eV

Electron-hole puddle distribution shows the electron accumulation around hole regions where p_z orbital is hydrogenated. Once more incident wave with energy -0.77 eV in this region is solved time dependently within TB model. This time, because of the greater number of impurity states, the wave is severely localized. Third region in 3.17, where

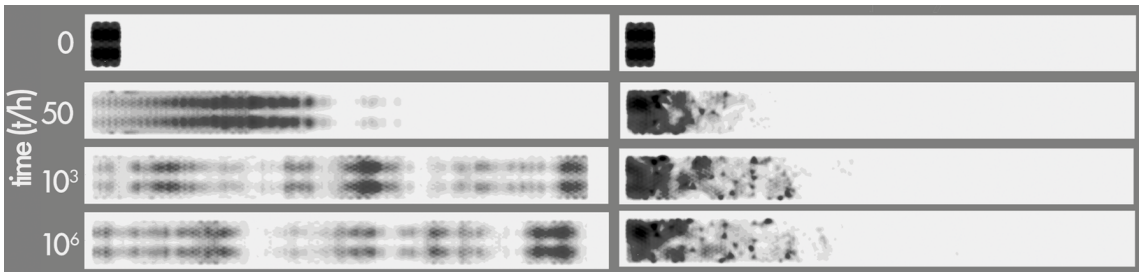

Figure 3.20. Clean (left) and disordered (right) time dependent solution of wave function dispersion within second region with incident particle energy -0.74 eV

zero energetic edge states can be found. Puddle formation shows mostly fractured edge states with some impurity states and according to the time dependent solution wave diffusive wave does not leave the edge states. This time, energy of the initial wave is 0.22eV. Similar to the second region, even though it is not severe as that region, wave is localized. Localization in this region mostly occurs in 1D because motion along zigzag edges can be considered as an atomic chain. Forth region in Figure 3.10 is the lowest conduction

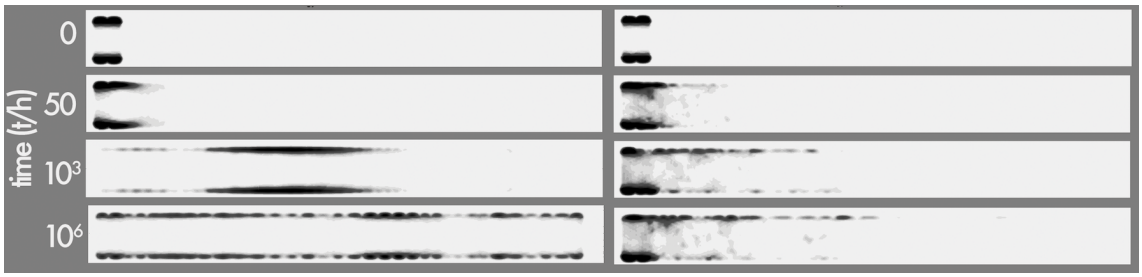

Figure 3.21. Clean (left) and disordered (right) time dependent solution of wave function dispersion within third region with incident particle energy 0.22 eV

state where no impurity state can be found. Electron hole puddle formation shows some localization, but it is mostly homogeneous, which signals that, localization in this region is weak. Finally time dependent solution with incident energy 1.046 eV shows that wave is not localized as its valence corresponding part (second region). This is mainly because of the absence of impurity states within this region.

To get numerical result for localization, a convenient way is to sum the quasistationary density along the longitudinal direction and take the time average to make plot as smooth as possible. For this part, time it takes to reach quasistationary state is chosen

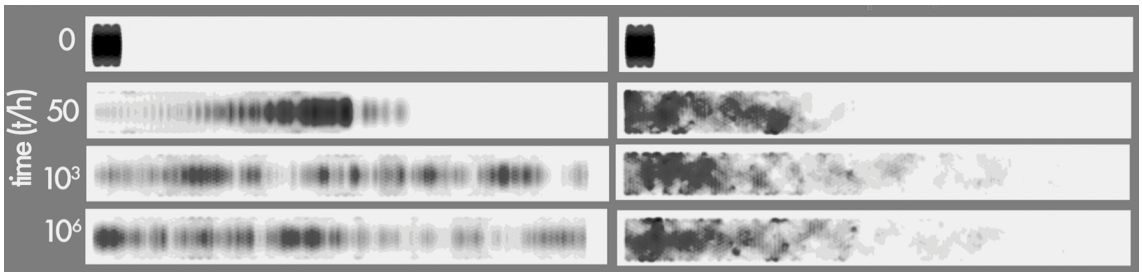

Figure 3.22. Clean (left) and disordered (right) time dependent solution of wave function dispersion within fourth region with incident particle energy 1.05 eV

as $t = 10^6/\hbar$ with average is taken in 10 steps around this point. Figure 3.23 shows the localization length for all four regions. It is a direct evidence that, localization is more severe around the Fermi level and it becomes weaker going into to deep level states. Other conclusion is that, hydrogenation of graphene mostly disturbs transport within valence band. Thus localization is more drastic in this region. However, within conduction band, localization loses its effect and transport in this region is less demanding.

In conclusion, for finite zigzag graphene nanoribbon Anderson localization induced metal-insulator transition is observed by solving time dependent tight binding model. We found that hydrogenation effect is severe around the Fermi level in agreement with earlier theoretical work[41]. In addition to these we concluded, transport in valence states are more vulnerable to hydrogenation effects.

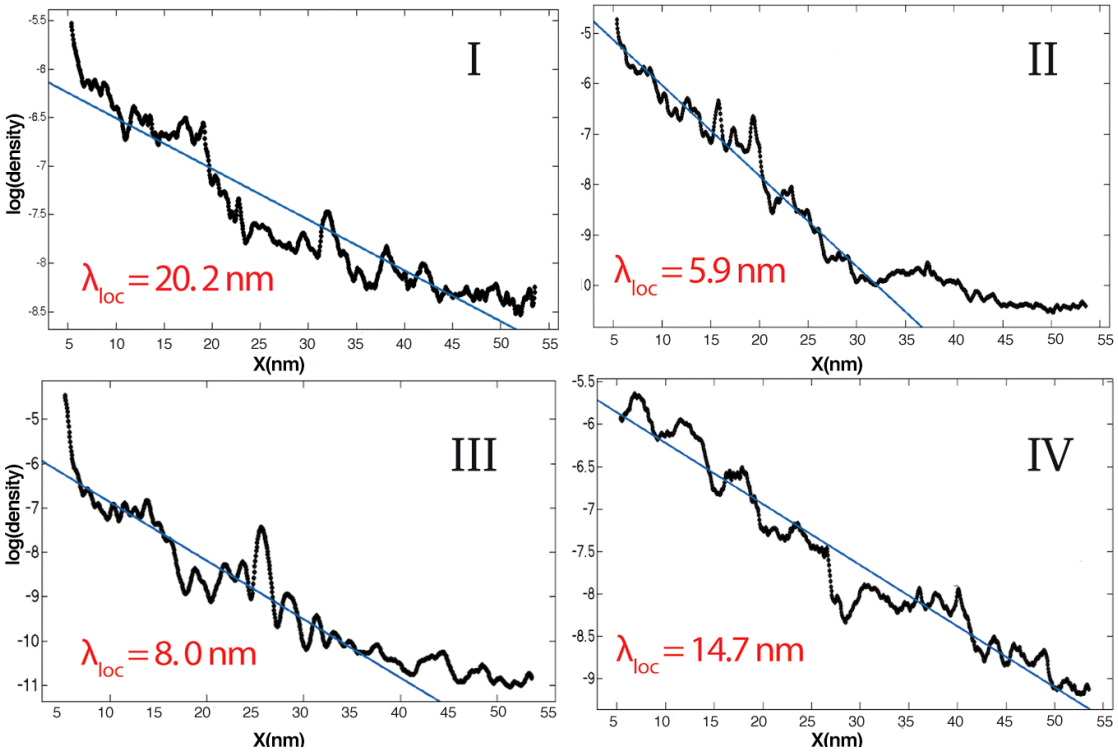

Figure 3.23. Time average solution with quasistationary states. Densities are summed along y direction and slope of the corresponding fits gives approximate information about localization length. Anderson localization mostly occurs around Fermi level as expected and loses its strength while going to deep level states. It is also inferred that, wave are more localized moving through valence band because of the impurity states.

CHAPTER 4

CONCLUSIONS

To conclude, we have investigated electronic, magnetic and optical properties of graphene nanoribbons in finite and cyclic topology. For the both structures, combined effect of electron-electron interactions and random potential fluctuations on the stability of edge states and magnetic phases is studied. The electronic stability of edge states is found to be surprisingly robust against disorder due to electron-electron interactions. Moreover, as the disorder potential strength is increased, the system goes through an antiferromagnetic-to-ferromagnetic phase transition, in agreement with the experimental results of Ref.[20] Although the possibility of such a transition is well known from previous calculations for a doped system, here, the nanoribbon is charge neutral. Thus the magnetic transition is due to local charge doping regions.

Due to topological constraints some of the calculations are only performed in finite structure. First one of these is determination of optical characteristics under impurity effects. In this part, interplay between electronic and optical properties are investigated. It was found that due to quantum confinement effect, light absorption characteristics are different for diffent polarization orientations. Also, by comparing the TB and MFH results it was found that electronic interaction effects makes universal optical conductance robust against disorder and peak around Fermi level in TB calculations always washed out by including the electronic interaction effects. Since impurities lift the degeneracy, oscillations in optical conductance smoothens by these effects. Spin dependent calculations are also enabled us to investigate optical absorption for different magnetic phases. We concluded that, interaction between two bulk-edge mix states in FM phase induce a peak very next to Fermi level which is absent in AFM phase. We concluded this result, gives a potential characterization method for to determine the magnetic phase of the nanoribbon. However, since mean field theory is not accurate around proximity of Fermi level further studies those take electron-electron interaction effects are needed to verify this result.

Other part constrained by the geometry is the investigation of metal insulator transition due to impurity effects. We found that impurity states tend to accumulate around $[-0.5, 0eV]$ interval. Due to these states, localization length is shorter compared to other DOS regions. Even though it was earlier known that states around Fermi level are much more vulnerable to localization, in this study we showed that hydrogenation of graphene effects mostly hole transport within valence band, compared to conduction.

APPENDIX A

PUBLICATIONS

- H. U. Özdemir, A. Altıntaş, A. D. Güçlü, Magnetic Phases of Graphene Nanoribbons under Potential Fluctuations, Phys. Rev. B **93**, 014415 (2016).
- H. U. Özdemir, K. Çakmak, A. Altıntaş, A. D. Güçlü, Observation of Metal-Insulator Transition on Graphene Nanoribbons, 5th. Condensed Matter Meeting (YMF),Izmir, April 2016, Poster Presentation.
- H. U. Özdemir, A. Altıntaş, A. D. Güçlü, Electronic Interaction Effects on Graphene Nanoribbons, Photonics Workshop, ICTP-ECAR, August 2015, Poster Presentation.
- A. Altıntaş, H. U. Özdemir, A. D. Güçlü, Optical Properties of Graphene Quantum Dots, 4th. Condensed Matter Meeting (YMF), Izmir, April 2015, Poster Presentation.

REFERENCES

[1] Landau, L. D. Zur Theorie der phasenumwandlungen II. Phys. Z. Sowjetunion, **11**, 26-35 (1937).

[2] Peierls, R. E. Quelques proprietes typiques des corpses solides. Ann. I. H. Poincare **5**, 177-222 (1935).

[3] Mermin, N. D. Crystalline order in two dimensions. Phys. Rev. **176**, 250-254 (1968).

[4] Venables, J. A., Spiller, G. D. T. and Hanbucken, M. Nucleation and growth of thin films. Rep. Prog. Phys. **47**, 399-459 (1984)

[5] K. S. Novoselov, A. K. Geim, S. V. Morozov, D. Jiang, Y. Zhang, S. V. Dubonos, I. V. Grigorieva, and A. A. Firsov, Science **306**, 666 (2004).

[6] Wallace, P. R. The band theory of graphite. Phys. Rev. **71**, 622-634 (1947)

[7] Jannik C. Meyer, A. K. Geim, M. I. Katsnelson, K. S. Novoselov, T. J. Booth and S. Roth, Nature **446**, 60-63 (2007).

[8] K. S. Novoselov, A. K. Geim, S. V. Morozov, D. Jiang, M. I. Katsnelson, I. V. Grigorieva, S. V. Dubonos, and A. A. Firsov, Nature **438**, 197 (2005)

[9] A. H. C. Neto, F. Guinea, N. M. R. Peres, K. S. Novoselov, and A. K. Geim, Rev. Mod. Phys. **81**, 109 (2009).

[10] A. K. Geim and K. S. Novoselov, Nature Materials **6**, 183 - 191 (2007).

[11] K. von Klitzing, G. Dorda, and M. Pepper. Phys. Rev. Lett. **45**, 494 (1980).

[12] K. S. Novoselov, Z. Jiang, Y. Zhang, S. V. Morozov, H. L. Stormer, U. Zeitler, J. C. Maan, G. S. Boebinger, P. Kim, and A. K. Geim, Science **315**, 1379 (2007).

[13] O. Klein, Zeitschrift für Physik **53** (3-4), 157 (1929).

[14] M. I. Katsnelson, K. S. Novoselov, and A. K. Geim, Nature Physics textbf2, 620 (2006).

[15] M. Y. Han, B. Özyilmaz, Y. Zhang and P. Kim, Phys. Rev. Lett. **98**, 206805 (2007).

[16] L. Yang, C.-H. Park, Y.-W. Son, M. L. Cohen and S. G. Louie, Phys. Rev. Lett. **99**, 186801 (2007).

[17] X. Li, X. Wang, L. Zhang, S. Lee, H. Dai, Science **29**, 1229-1232 (2008).

[18] M. Fujita, K. Wakabayashi, K. Nakada, and K. Kusakabe, J. Phys. Soc. Jpn. **65** (1996).

[19] K. Nakada, M. Fujita, G. Dresselhaus, and M. S. Dresselhaus Phys. Rev. B **54**, 17954 (1996).

[20] G. Z. Magda, X. Jin, I. Hagymási, P. Vancsó, Z. Osváth, P. Nemes-Incze, C. Hwang, L. P. Biró, and L. Tapasztò, Nature **514**, 6611 (2014).

[21] Y.-W. Son, M. L. Cohen, and S. G. Louie, Phys. Rev. Lett. 97, 216803 (2006).

[22] J. Jung, T. Pereg-Barnea, and A. H. MacDonald, Phys. Rev. Lett. **102**, 227205 (2009).

[23] J. Jung, and A. H. MacDonald, Phys. Rev. B **79**, 235433 (2009).

[24] Y.-W. Son, M. L. Cohen, and S. G. Louie, Nature, **444**, 347-349 (2006).

[25] E. H. Lieb, Phys. Rev. Lett. **62**, 1927 (1989).

[26] M. Wimmer, I. Adagideli, S. Berber, D. Tomanek, and K. Richter. Phys. Rev. Lett. **100**, 177207 (2008).

[27] A. Kimouche, *et al.* Nat. Commun. **6** 10177 (2015).

[28] P. Ruffieux, S. Wang, B. Yang, C. SÃ¡nchez-SÃ¡nchez, J. Liu, T. Dienel, L. Talirz, P. Shinde, C. A. Pignedoli, D. Passerone, T. Dumslaff, X Feng, K. MÃ$\frac{1}{4}$llen and R. Fasel, Nature **531**, 489-492 (2016)

[29] P. Esquinazi, D. Spemann, R. HÃ¶hne, A. Setzer, K.-H. Han, and T. Butz, Phys. Rev. Lett. **91**, 227201 (2003).

[30] J. Fernandez-Rossier, and J. J. Palacios, Phys. Rev. Lett. **99**, 177204 (2007).

[31] L. Pisani J. A. Chan, B. Montanari, and N. M. Harrison, Phys. Rev. B **75**, 064418 (2007)

[32] O. V. Yazyev and L. Helm, Phys. Rev. B. **75**, 125408 (2007).

[33] X. Zhang, O. V Yazyev, J. Feng, L. Xie, C. Tao,Y. C. Chen, L. Jiao, Z. Pedramrazie, A. Zettl, S. G. Louie, H. Dai, and M. F. Crommie, ACS Nano **7** (1) (2013).

[34] J. Kunstmann, C. Özdoğan, A. Quandt, and H. Fehske, Phys. Rev. B **83**, 045414 (2011).

[35] P. Koskinen, S. Malola, and H. Häkkinen, Phys. Rev. Lett. **101**, 115502 (2008).

[36] P. Koskinen, S. Malola, and H. Häkkinen, Phys. Rev. B **80**, 073401 (2009).

[37] T. Wassmann, A. P. Seitsonen, A. M. Saitta, M. Lazzeri, and F. Mauri, Phys. Rev. Lett. **101**, 096402 (2008).

[38] J. Bundesmann, M. H Liu, I. Adagideli, and K. Richter, Phys. Rev. B **88**, 195406 (2013).

[39] E. Rossi and S. Das Sarma, Phys. Rev. Lett. **101**, 166803 (2008).

[40] S. Das Sarma, S. Adam, E. H. Hwang, and E. Rossi, Rev. Mod. Phys. **83**, 407 (2011).

[41] G. Schubert and H. Fehske, Phys. Rev. Lett. **108**, 066402 (2012).

[42] J. Martin, N. Akerman, G. Ulbricht, T. Lohmann, J. H. Smet, K. von Klitzing, and A. Yacoby, Nature Physics **4**, 144 - 148 (2008).

[43] Y. Zhang,V. W. Brar, C. Girit, A. Zettl, and M. F. Crommie, Nature Physics **5**, 722 - 726 (2009).

[44] M. Gibertini, A. Tomadin, F. Guinea, M. I. Katsnelson, and M. Polini, Phys. Rev. B 85, 201405(R) (2012).

[45] M. Polini, A. Tomadin, R. Asgari, and A. H. MacDonald, Phys. Rev. B **78**, 115426 (2008).

[46] P.J. Mohr, B.N. Taylor, and D.B. Newell (2015), (Web Version 7.0). This database was developed by J. Baker, M. Douma, and S. Kotochigova. Available: http://physics.nist.gov/constants, National Institute of Standards and Technology, Gaithersburg, MD 20899.

[47] R. R. Nair, P. Blake, A. N. Grigorenko, K. S. Novoselov, T. J. Booth, T. Stauber, N. M. R. Peres, A. K. Geim, Science **320** (5881), 1308 (2008)

[48] R. Bouchendira, P. Clade, S. Guellati-Khelifa, F. Nez, and F. Biraben, Phys. Rev. Lett. **106**, 080801 (2011).

[49] A. S. Pavlova, E. A. Obraztsova, A. V. Belkin, C. Monat, P. Rojo-Romeo ; E. D. Obraztsova, J. Nanophoton. **10(1)**, 012525 (2016).

[50] C. Berger, Z. Song, X. Li, X. Wu, N. Brown, C. Naud, D. Mayou, T. Li, J. Hass, A. N. Marchenkov, E. H. Conrad, P. N. First, W. A. de Heer, **312**, 5777 (2006).

[51] T. Ohta, F. E. Gabaly, A. Bostwick, J. L. McChesney, K. V. Emtsev, A. K. Schmid, T. Seyller, K. Horn and E. Rotenberg, New Journal of Physics **10**, 023034 (2008).

[52] C. Virojanadara, M. Syvajarvi, R. Yakimova, L. I. Johansson, A. A. Zakharov, and T. Balasubramanian, Phys. Rev. B **78**, 245403 (2008).

[53] D. V. Kosynkin, A. L. Higginbotham, A. Sinitskii, J. R. Lomeda, A. Dimiev, B. K. Price, and J. M. Tour, Nature **458**, 872-876 (2009)

[54] X. Wang and H. Dai, Nature Chemistry **2**, 661-665 (2010).

[55] Q.X. Pei, Y.W. Zhang, V.B. Shenoy, Carbon **48**, 898-904 (2010).

[56] A. D. Güçlü, P. Potasz, O. Voznyy, M. Korkusinski, P. Hawrylak, Phys. Rev. Lett. **103**,

246805 (2009).

[57] A.D. Güçlü, **arXiv**: cond-mat.mes-hall/1510.05913v1 (2015).

[58] O. V. Yazyev, M. I. Katsnelson, Phys. Rev. Lett. **100**, 047209 (2008).

[59] K. Wakabayashi, M. Sigrist, and M. Fujita, J. Phys. Soc. Jpn. **67**, 2089 (1998).

[60] B. Wunsch, T. Stauber, F. Sols, F. Guinea, Phys. Rev. Lett. **101** 036803 (2008).

[61] A. Yamashiro, Y. Shimoi, K. Harigaya, and K. Wakabayashi, Phys. Rev. B **68**, 193410 (2003).

[62] O. V. Yazyev, R. B. Capaz, and S. G. Louie, Phys. Rev. B **84**, 115406 (2011).

[63] H. Feldner, Z. Y. Meng, A. Honecker, D. Cabra, S. Wessel, and F. F. Assaad, Phys. Rev. B **81**, 115416 (2010).

[64] W. L. Wang, O. V. Yazyev, S. Meng, and E. Kaxiras, Phys. Rev. Lett. **102**, 157201 (2009).

[65] J. Cao and S.-J. Xiong, Phys. Rev. B **88**, 085409 (2013).

[66] W. Jaskolski, L. Chico, A. Ayuela, Phys. Rev. B **91**, 165427 (2015).

[67] A. R. Carvalho, J. H. Warnes, and C. H. Lewenkopf, Phys. Rev. B **89**, 245444 (2014).

[68] A. D. Güçlü, M. Grabowski, and P. Hawrylak, Phys. Rev. B **87**, 035435 (2013).

[69] N. A. Poklonski, E. F. Kislyakov, S. A. Vyrko, O. N. Bubel S. V. Ratkevich, J. Nanophoton. **6**(1), 061712 (2012).

[70] K. F. Mak, L. Ju, F. Wang, T. F. Heinz, Solid State Communications **52**, 1341-1349 (2012).

[71] J. Horng, C.-F. Chen, B. Geng, C. Girit, Y. Zhang, Z. Hao, H.A. Bechtel, M. Martin, A. Zettl, M.F. Crommie, Y.R. Shen, F. Wang, Phys. Rev. B **83** (2011) 165113.

[72] P. Potasz, A.D. Güçlü, P. Hawrylak, Phys. Rev. B **82**, 075425 (2010).

[73] A. Einstein, Annalen der Physik (in German) **322** (8), 549-560 (1905).

[74] P. W. Anderson, Phys. Rev. 109 **5**, 1492-1505 (1958).

[75] D. J. Thouless, J. Phys. C: Solid State Phys. **4**, 1559 (1970).

[76] P. W. Anderson, Rev. Mod. Phys. **50**,191 (1978).

[77] H. G. Schuster, Z. Physik B **31**, 99 (1978).

[78] E. Abrahams, P. W. Anderson, D. C. Licciardello and T. V. Ramakrishnan, Phys. Rev. Lett. **42**, 673 (1979).

[79] S. Hikami, A. I. Larkin and Y. Nagaoka, Prog. Theor. Phys. **63**, 707 (1980).

[80] F. Evers, A. Mirlin, Rev. Mod. Phys, **80** 1355 (2008)

[81] A. Bostwick **et al.**, Phys. Rev. Lett. **103**, 056404 (2009).

[82] L. A. Ponomarenko **et al.**, Nature Phys. **7**, 958 (2011).

[83] A. L. Magna, I. Deretzis, G. Forte, R. Pucci, Phys. Status Solidi C **7**, No. 3-4, 1246-1250 (2010)

[84] E. R. Mucciolo, H. C. Neto, and C. H. Lewenkopf, Phys. Rev. B **79**, 07540720 (2009)

[85] A. Pieper, G. Schubert, G. Wellein, and H. Fehske, Phys. Rev. B **88**, 195409 (2013)

[86] S. Adam, S. Cho, M. S. Fuhrer, and S. Das Sarma, Phys. Rev. Lett, **101**, 046404 (2008)

[87] A.D. Güçlü, P. Potasz, M. Korkusinski, P. Hawrylak, Graphene Quantum Dots, Springer, Berlin, Heidelberg, 2014.

[88] P.A.M. Dirac, Proc. of the Royal Soc. A **114** (767): 243-265 (1927).